POLARIZABILITY AND REFRACTIVITY OF GASES IN THERMOCHEMICAL NONEQUILIBRIUM

A Thesis

by

NICHOLAS SIMION MANAVI

Submitted to the Graduate and Professional School of
Texas A&M University
in partial fulfillment of the requirements for the degree of

MASTER OF SCIENCE

Chair of Committee,	Albina A. Tropina
Co-Chair of Committee,	Richard B. Miles
Committee Member,	Waruna D. Kulatilaka
Head of Department,	Ivett A. Leyva

December 2022

Major Subject: Aerospace Engineering

ABSTRACT

The physics of hypersonic flight is challenging due to the high-temperature environment and presence of chemical and vibrational nonequilibrium. Hypersonic flow over a blunt wedge body is studied for different chemical species, each individually present in air. A semi-classical quantum mechanical model, which calculates the polarizability as a function of the translational and vibrational temperature, is used. The temperature fields from simulated nitrogen, oxygen, and argon flows are used to find the polarizability and refractive index fields. Experiments are performed in the Hypervelocity Expansion Tunnel at various Mach numbers and flight conditions corresponding to altitudes ranging from 35,000 to 45,000 feet. A Michelson interferometer with significant reference mirror tilt is used to generate static interferograms to measure the phase difference. The resultant refractive index fields are compared directly to the model to analyze thermochemical nonequilibrium effects. An uncertainty analysis of the experimental data was performed to understand any observed deviations from the model.

DEDICATION

To my mother and father, Mihaela and Paul Manavi, for guiding me towards success in every step of my life.

ACKNOWLEDGMENTS

It takes a village to raise a graduate student, and I am grateful for the teachings from my co-advisors: Dr. Tropina and Dr. Miles. I see them as my graduate parents at Texas A&M, supporting me through my journey towards becoming a better researcher, both experimentally and theoretically. Dr. Tropina has been my main source of assistance when it comes to theoretical issues regarding the propagation of light waves and numerical simulations for the experiment. Dr. Miles has helped guide me in finding realistic approaches of acquiring data with an interferometer. I would not have made it without both of their help.

I would also like to thank the people who mechanically supported my experiment in the ALLEMO lab. Firstly Kevin Brown, who was the laser technician introducing me to the basics of hands-on experimental optics. I watched and assisted him in reassembling PBL-0, bringing the old laser, previously decommissioned from an old Princeton experiment, back to life for the purpose of the proof-of-concept. He emphasized the importance of safe practices when operating the laser, and I would not be capable of running the experiment independently without his careful help and attention. I would also like to thank John Kochan, who helped in the design and construction process for the interferometer, providing much-needed mechanical advice for the interferometer. I would like to thank James Creel for offering his advice and support for the experiment, specifically on how to properly use the very expensive lab camera. I would also like to thank Tyler Dean and Donovan McGruder, two PhD students at the NAL, for helping me schedule and run my experiment in the HXT.

My work will be built upon another MS, Juan Anaya, who helped me through a lot of hardships during my final test campaign. His help was also important to collecting high-quality fringe data, and his future work will be important to putting the pieces of this project together.

I would like to thank Dr. Felipe Guzman, Dr. Christopher Limbach, and Dr. Waruna Kulatilaka for taking the time to review certain stages of the experiment and offer advice for good practices.

CONTRIBUTORS AND FUNDING SOURCES

Contributors

This work was supported by a thesis committee consisting of Professor Albina Tropina, my primary advisor, and Dr. Richard Miles, my secondary advisor, both of the Department of Aerospace Engineering, and Professor Waruna Kulatilaka of the Department of Mechanical Engineering.

Experimental data collection was performed with assistance from Kevin Brown, James Creel, and Tyler Dean for test campaign 1. Data collection was also performed with assistance from Donovan McGruder and Tyler Dean for test campaign 2. Data collection was also performed with assistance from Tyler Dean, Donovan McGruder, and Juan Anaya for test campaign 3. The theoretical model used was originally developed by Dr. Tropina and modified for use in the present work.

All other work conducted for the thesis was completed by the student independently.

Funding Sources

This work was supported by internal funds from the Texas A&M University Aerospace Engineering Department and the AFRL.

NOMENCLATURE

AFRL	Air Force Research Lab
ALLEMO	Aerospace Laboratory for Lasers, ElectroMagnetics, and Optics
DMS	Direct Molecular Simulation
FFT	Fast Fourier Transform
FOV	Field of View
HXT	High-speed Expansion Tunnel
IDEA	Interferometric Data Evaluation Algorithms
IR	Infrared
NAL	National Aerothermochemistry and Hypersonics Laboratory
NIST	National Institute of Standards and Technology
OPD	Optical Path Difference
OPL	Optical Path Length
PBL	Pulse Burst Laser
PSI	Phase Shifting Interferometer
TAMU	Texas A&M University

TABLE OF CONTENTS

Page

LIST OF FIGURES

FIGURE Page

LIST OF TABLES

TABLE Page

1. INTRODUCTION

Air is composed almost entirely of diatomic Nitrogen and Oxygen, and a small portion of what remains is Argon. The air composition changes at hypersonic speeds, since the high temperatures lead to dissociation of molecular oxygen and nitrogen and appearance of atomic species O and N, which recombine to form nitric oxide (NO). Furthermore, the high speed air experiences not only chemical but also vibrational nonequilibrium. Each component of air can be studied to gain a clear understanding of how the refractive index changes due to thermochemical nonequilibrium in pure Nitrogen, Oxygen and Argon flows.

The refractive index quantifies how light changes phase when passing through a medium. This metric is essential for laser diagnostics to characterize optical properties of the medium. Corrections due to optical disturbances are important to take accurate measurements from a hypersonic vehicle, or to take measurements as a stationary observer. The refractive index can be used to measure temperature, concentration and find other properties of the flow, which can be found by understanding how the phase of light changes in the medium compared to a vacuum. The refractive index depends on the composition and polarizability of the medium. A measure of the polarizability in nonequilibrium flow has not been at the forefront of other hypersonic studies, but recent work from Tropina [1] shows a theoretical model, used in the present work, that can account for vibrational nonequilibrium effects.

1.1 Theoretical Background

This section introduces concepts important to understanding how to model the polarizability and refractive index behind a strong shockwave. There is extensive work dating back to the 1960s describing properties behind inviscid blunt body high speed flows. Important to the current theoretical framework is an understanding of some basic concepts in quantum mechanics and spectroscopy, which are also reviewed in this section.

1.1.1 Hypersonic flow conditions

A strong understanding of the fundamentals of hypersonic flows is important, since the models use a number of assumptions about the flow which should be taken into account when considering the real experimental conditions. For example, in a chemically reacting mixture of perfect gases, the first few milliseconds of the high speed flow are generally characterized by a time dependent changes of the chemical composition and temperature, which is referred to as thermochemical nonequilibrium. Since the experimental shock tube only creates hypersonic conditions on the order of a few milliseconds, it is possible that even sections of the flow that are simulated to be in thermochemical equilibrium actually do not have enough time to reach that state. For more detail, Anderson does an excellent job developing basic concepts of hypersonic flows and related nonequilibrium phenomena [2].

According to the Boltzmann theory, temperature is the measure of the average kinetic energy of particles at some point in space. Due to the momentum and kinetic energy exchange in elastic collisions between particles, if there are no collisions, the temperature can not increase. Oxygen molecules should take approximately 20,000 collisions to reach their vibrationally excited states, with dissociation occurring on the order of 200,000 collisions. This is similarly true for chemical reactions, which occur, when particles collide. This effect is more pronounced in flows with high pressure and low temperature, since the collision frequency $Z \propto \frac{p}{\sqrt{T}}$.

An important consideration for hypersonic flows is the reaction time. Equilibrium flow implies infinite chemical and thermal reaction rates leading to the same energy (temperature) for all components of the flow. It means that gas has enough time to bring all internal degrees of freedom to equilibrium with the translational energy of molecules, which move. By contrast, so called vibrationally frozen flow implies zero chemical and thermal reaction rates, when gas composition and temperature changes so fast but the vibrational energy is practically constant. At hypersonic speeds, there is not enough time for the gas to reach equilibrium state. Thus we can see thermal and chemical nonequilibrium, which often occurs immediately after the shock front. This is the location where transport phenomena of viscosity and thermal conduction are important, since there

is a large temperature, velocity, and pressure gradient there. The distance required for the flow to reach equilibrium after the shock front is referred to as the relaxation distance. Depending on the geometry of the surface and the location of the streamline, the relaxation distance will change. Moving across a normal shockwave leads to a shorter relaxation distance and a larger temperature gradient after the shock front, compared to crossing an oblique shockwave. Time to reach equilibrium state for a gas in a vibrational nonequilibrium is called the vibrational-translational relaxation time and it depends on the temperature, pressure and gas itself. Vibrational-translational relaxation times for Oxygen, Argon, and Nitrogen are presented in [3].

The relationship between air composition and temperature are shown by Anderson [2](pg.459-460). At an air temperature around T=800 K, vibrational excitation starts becoming significant. At temperatures around T=2500 K, Oxygen begins to experience significant dissociation, until it is fully dissociated at T=4000 K. Nitrogen gas begins to dissociate at temperatures around T=4000 K and becomes fully dissociated at T=9000 K, when both Nitrogen and Oxygen ions begin forming. Figure 1.1 depicts changes in the air composition depending on the gas temperature, adapted from [2].

Equilibrium composition in a high speed flow can be found via the law of mass action, which describes conservation of particles in a system in terms of reaction rates. Chemical reactions occurring after the shockwave lead to much larger density ratios than those predicted by isentropic supersonic flows. Because of this, the shockwave detachment distance from the body is typically much smaller and the shock layer is much thinner in a hypersonic flow compared with the supersonic flow. Furthermore, for example, the blunt-body shockwaves for hypersonic flows have a $\theta - \beta - V$ analogue of the well-known $\theta - \beta - M$ relationship of supersonic flows. In nonequilibrium flows, importance of the Mach number is even less significant to understand gas properties after the shockwave. The impact of the high velocity is represented in the enthalpy of the system, which is an important variable to characterize properties of the hypersonic flow.

Although chemical equilibrium and thermal nonequilibrium are separated, they are almost always seen together in hypersonic flows. This leads to complexity with analysis since the thermo-

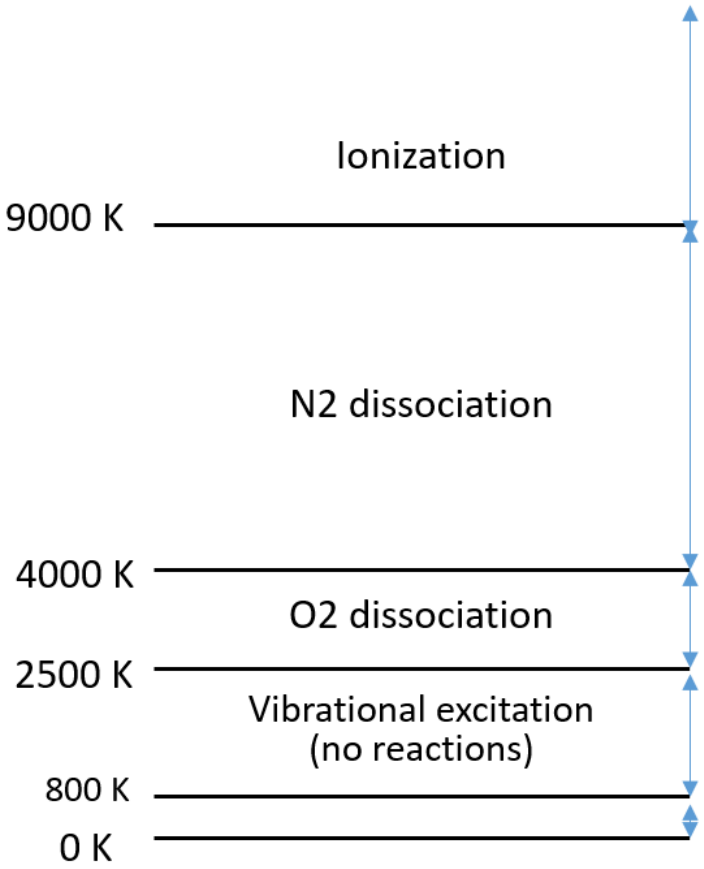

Figure 1.1: Changes in the air composition depending on the temperature

chemical reactions are coupled, they depend not only on the translational but also on the vibrational temperature, increasing the non-linearity of the system.

Hypersonic flows over blunt-bodies contain regions with varying temperature fields and air compositions. Laser propagation through such media results in relative changes in refractive index due to vibrational nonequilibrium and composition changes. Those differences can be isolated and explored within a single image. A unique property of flows over a blunt-nose body is that the gas expands to form a curved shock layer, which reduces the post-shock reaction rates. For example, simulations at conditions of high altitudes (150,000-250,000ft) and velocities (15,000-23,000$\frac{ft}{s}$) were run to explore nonequilibrium properties of the flow over a blunt body by Hall et al. [4]. It was shown that regions with the vibrational nonequilibrium and dissociation can be found near the

nose of a blunt body hypersonic wedge. In this work, those regions with vibrational nonequilibrium and dissociation are explored in detail using interference patterns for the high enthalpy, high speed flows.

Numerical observations of the effects of thermochemical nonequilibrium on the refractive index has already been performed to some extent by Mackey and Boyd [5]. These simulations predicted at least a 2% change in the refractive index in high enthalpy flows due to vibrational nonequilibrium, up to 5% in Mach 15 flows. These numerical simulations are a good baseline to start from, since a 2% difference should be detected within a well-designed interferometer setup.

1.1.2 Conceptualizing polarizability

In hypersonic flows, the high temperatures lead to a significant number of reactions and nonequilibrium effects which require quantum-mechanical models to properly predict and simulate gas flow properties and reactions rates. One of the important metrics for these microscopic effects is the polarizability. The polarizability is a measure of the electric dipole moment that appears under the action of an external electric field on a gas molecule or an atom, leading to the charge separation of electrons from the nucleus. In general the polarizability can be represented as a 3x3 tensor, where diagonal elements describe the molecule/atom response parallel to the applied electric field. For a spherically symmetrical charge distribution, the average molecular polarizability can be introduced as an average of the sum of the diagonal elements. In this work, only the electric dipole polarizability will be considered, where the alternating electric field will be a function of the laser wavelength. Much of the information in this section is reviewed in the following textbook [6].

The quantum harmonic oscillator model explaining vibrational states of the molecule is used in the present work. Because the mass of the nucleus surpasses that of the electron enough to be considered an immovable object from the electron's perspective, the electron is modeled as a mass on a spring. The spring force between the nucleus and the electron is represented by their bond. The induced oscillation of electrons comes from an external electromagnetic field. This proves to be a good assumption, particularly for lower-lying energy levels of molecules, such as the ground state. The harmonic oscillator theory starts to break down only when reaching high energy states

near the ionization energy level, where an anharmonic oscillator model almost perfectly corrects for these differences. To explain excitation of rotational levels the model of the diatomic molecule as a rigid rotor is used. As a result both rotational and vibrational energy levels of a molecule can be calculated using Dunham coefficients from the NIST data base. This semi-classical representation of the internal energy levels of the diatomic molecule is the base of the polarizability model used in this work.

1.1.3 Development of semi-classical polarizability model

Preliminary work was carried by Tropina to develop a model to predict how the polarizability and refractive index changes depending on the level of vibrational nonequilibrium [1]. The theoretical model was validated using a sparse amount of preexisting experimental research. This provided credibility to the model, but more experiments from high enthalpy flows will provide greater confidence in the validity and the limits of the model. This semi-classical model was used to calculate the polarizability and refractive index using the translational and vibrational temperature distribution. The model is based on the representation of the total energy of a molecule as the sum of the electronic energy, the vibrational energy, and the rotational energy:

$$E = E_e + E_\nu + E_r \tag{1.1}$$

To get an expression for the polarizability, an electron can be modeled as a driven simple harmonic oscillator, attached to a massive nucleus by a springlike mechanism. The second order differential equation, explaining the electron motion in an electric field, is as follows :

$$\begin{aligned} m_e \tfrac{d^2x(t)}{dt^2} + \gamma m_e \tfrac{dx(t)}{dt} + Kx(t) &= -qe_x(t) \\ \text{where } w_0^2 &= \tfrac{K}{m_e} \\ \frac{d^2x(t)}{dt^2} + \gamma\frac{dx(t)}{dt} + w_0^2 x(t) &= -\frac{q}{m_e}e_x(t) \end{aligned} \tag{1.2}$$

where m_e is the mass of the electron, x is the position of the electron, γ is the damping coefficient of the oscillator, K is the spring constant, q is the charge of the electron, e_x is the driving

electric field, and w_0 is the resonant frequency of the oscillator. Assume the displacement field and the driving field are both sinusoidal. After substituting them into Eq. 1.2, an expression for the displacement as a function of the frequency is formed, as shown below:

$$\begin{aligned} e_x(t) &= \epsilon_x(\omega)\exp(-i\omega t) \\ x(t) &= X(\omega)\exp(-i\omega t) \end{aligned}$$

$$X(\omega) = \frac{q}{m}\left(\frac{\epsilon_x(\omega)}{(\omega^2-\omega_0^2)+i\gamma\omega}\right) \tag{1.3}$$

The dipole moment of each oscillator is defined in the frequency domain:

$$\Psi(\omega) = -qX(\omega) \tag{1.4}$$

The polarization field can then be found to be influenced by a certain N oscillators per unit volume. This number N is the number density of particles. The summed effects of all dipole moments within a unit volume is used to define the polarizability in a specific volume.

$$\alpha(\omega) = N\Psi(\omega) \tag{1.5}$$

Substituting the equations above generates the following equation for the polarizability:

$$\alpha(\omega) = \frac{Nq^2}{m}\left(\frac{\epsilon_x(\omega)}{(\omega_0^2-\omega^2)-i\gamma\omega}\right) \tag{1.6}$$

This equation is still written in terms of a classical harmonic oscillator. The Schrodinger wave equation solution for a simple harmonic oscillator only allows for energy transitions between the immediately higher or lower rotational/vibrational level; all other transitions are prohibited. To convert this oscillator to a two-level quantum system, a few changes should be made to the above equation:

1. The resonant frequency term, ω_0, is replaced by the transition frequency,ω_{12}, between energy levels. This frequency is defined in terms of the energy difference between levels: $w_{12} =$

$\frac{E_2 - E_1}{\hbar}$

2. The damping constant is replaced by the state relaxation rate $\gamma \rightarrow \gamma_{21}$

3. The strength of the transition is represented by the oscillator strength, $\epsilon_x \rightarrow f_{12}$

4. The number density of oscillators is replaced by the population difference, $N \rightarrow N_1 - N_2$

Applying these changes to the equation yields the following semi classical model for the polarizability, relating to only a single state transition:

$$\alpha_{12}(\omega) = \frac{(N_1 - N_2)q^2}{m}\left(\frac{f_{12}}{(\omega_{12}^2 - \omega^2) - i\gamma_{21}\omega}\right) \tag{1.7}$$

ω is the laser frequency. Note that this formula takes into account only a single transition between the ground and excited electronic state of the particle. To get a full model of the polarizability of the molecule, input from all transitions from the ground state to electronically exited states below the ionization (dissociation) limit must be summarized. Thus changes in the population of vibrational and rotational states should influence the molecular polarizability. To complete the model, an accurate set of oscillator strengths for different transitions must be known. The oscillator strengths for the transitions from vibrational levels of the ground state are difficult to find in the literature, and the oscillator strengths for the transitions from rotational levels of the ground state prove to be an even greater challenge due to how many rotational levels exist for each vibrational level. In this work, the set of oscillator strengths from Zipf et al [7] and Chan [8], are used for nitrogen, and a combination of oscillator strengths from Huebner [9] and Chan [10] and Franck-Condon factors from Krupenie [11] are used for Oxygen. This approach is connected with the fact that the Franck-Condon factors represent the overlap between electron wavefunctions at the ground and excited electronic state, and the oscillator strength is introduced as a characteristic of such overlap. Thus, to find the unknown oscillator strengths the same multiplier to all Franck-Condon factors can be used.

The next development of this theory is related to a number density N for the specific excited

state. The population fraction ρ_g was used to represent the probability of the particle occupying a certain state g. Each vibrational and rotational state transition has a probability such that $\sum_0^\infty \rho = 1$. The population density is represented by the following:

$$\rho_g = \frac{\Gamma}{\sum_{\nu,J} \Gamma} \tag{1.8}$$

$$\Gamma = (2J+1)\exp(\frac{-E(\nu,J)}{k_B T}) \tag{1.9a}$$

The values for J are limited to 1 for odd rotational states and 2 for even rotational states, since these represent the allowed rotational transitions. The vibrational and rotational levels are assumed to be separately thermalized with different temperatures, so this changes the value for Γ to:

$$\Gamma = (2J+1)\exp(\frac{-E_\nu(\nu)}{k_B T})\exp(\frac{-E_J(J)}{k_B T}) \tag{1.9b}$$

For each of these states g, the sum of product between the known oscillator strengths for the energy level transitions and the population fraction at that state needs to be calculated to find the contribution to the total polarizability. The polarizability can then be found with the following:

$$\alpha(\omega) = \frac{q^2}{m_e} \sum_{g=0}^{g=\infty} \sum_{i=0}^{i=\infty} \frac{\rho_g f_{g,i}}{\omega_{g,i}^2 - \omega^2 - i\gamma_{i,g}\omega} \tag{1.10a}$$

This equation can be reduced if we assume the frequency response is far from resonance. Far from $\omega = \omega_0$, the damping term $i\gamma_{21}\omega$ can be ignored. So the final equation for the molecular polarizability becomes:

$$\alpha(\omega) = \frac{q^2}{m_e} \sum_{g=0}^{g=\infty} \sum_{i=0}^{i=\infty} \frac{\rho_g f_{g,i}}{\omega_{g,i}^2 - \omega^2} \tag{1.10b}$$

The polarizability is found here based on a number of assumptions about the molecule. The biggest obstacle of this model is finding an accurate set of oscillator strengths $f_{g,i}$ for each transition, especially for molecules with a large number of vibrational states. Uncertainty of the model,

which is assumed to be negligible, is connected with the fact that it does not take into account rotational nonequilibrium. Another uncertainty of the model is connected with an additional term added for higher lying electronic transitions with unknown oscillator strengths. .

It is desirable to validate the model using experimental measurements, particularly since there are numerous assumptions with the model. The index of refraction is relatively easy to measure with a high degree of certainty in a laboratory environment. To relate the refractive index, a macroscopic quality, to the polarizability, a microscopic quality, the Lorentz-Lorenz relation can be used.

$$\frac{n^2-1}{n^2+2} = \frac{4\pi}{3} N\tilde{\alpha}, \tag{1.11a}$$

where N is the number density of the medium and $\tilde{\alpha}$ is the polarizability volume. The polarizability volume relates to the average molecular polarizability through the unit conversion, such as $\tilde{\alpha} = \frac{\alpha}{4\pi\epsilon_0}$. This equation was initially founded by Lorenz, a Danish optical physicist, and Lorentz, a Dutch physicist, independent of each other and a decade apart. Lorenz derived the equation using available experimental data, while Lorentz derived this relation based on the Clausius-Mossotti formula combined with the electromagnetic theory of light. Information on the derivation of this law and analysis of main assumptions important to extreme cases, is given in [12] and [13]. Because the refractive index is not so different from 1, this equation can be re-written as shown below

$$n^2 \approx 1 + 4\pi N\tilde{\alpha} \tag{1.11b}$$

and finally

$$n \approx 1 + 2\pi N\tilde{\alpha} \tag{1.11c}$$

Now the refractive index, a quantity that can be experimentally measured, can be used to verify the model for polarizability and understand an effect of thermal and chemical nonequlibrium in a hypersonic flow. The following work only examines diatomic freestream test gases such as nitrogen and oxygen and their dissociated components in high-temperature and high speed flows.

This approach allows the problem to be broken down into its constituent parts before considering the hypersonic flow of air.

1.2 Experimental work

This section provides background information related to experimentation. The information in this section is about the experimental approach used such as interferometry. An explanation of the current work's experimental method is explained, and review of some interferometric measurements in hypersonic flows is presented.

1.2.1 Interferometry and refractive index measurements in a hypersonic flow

Relevant work includes the results from the paper of Boyce, who used interferometry to validate CFD simulations results in a 3D flow field [14]. Interferograms were captured in a hypersonic shock tube, and the measured density, extrapolated from the refractive index measurements, matched well with the predictions of CFD calculations. The studied conditions were at M=13 and T=110K. The temperature is significantly lower than what is encountered in nature, which means real hypersonic velocities will not be fully reached. In a recent work Psota [15] details a design of a Mach-Zehnder model to measure the density in hypersonic flows, which can be easily assembled using fiber optics. Another experimental measurement of the hypersonic flow density were presented by Desse and Fabre [16], which used a Wollaston prism to measure the refractive index. This study observed a flow at M=10 and T=50 K, which also indicates the post-shock flow velocity will be significantly different than experienced in nature. These low-enthalpy studies emphasize the lack of information available for high-enthalpy hypersonic flows in the vailable literature.

The work from Desse and Fabre also provided an example of double-pass interferoemtry being conducted over an axisymmetric body. This study is an example of measuring the refractive index with a system sensitive to retrace errors, which is true for the Michelson interferometer in the current work. Retrace errors occur because the beam must be aligned to retrace its exact path on return. This issue is not present for Mach-Zehnder interferometers, which only pass through a section once without requiring a retraced path. A Michelson interferometer is beneficial because

the test arm passes through the measured area twice. This doubles the optical path, allowing for changes in phase to be more apparent. This is especially useful for lower density flows, which are expected for the high Mach number experiments. But this method has the drawback of requiring precise alignment on the return beam to ensure high resolution data with a minimal error.

The main characteristics to describe the laser propagation in a medium are the optical path difference (OPD) and the optical path length (OPL). The OPL shows how long it takes for light to pass through a medium with a refractive index n on a certain distance. The optical path length can be defined in the integral form for the media with non-uniform refractive index

$$\text{OPL} = \int_a^b n(s)ds \tag{1.12a}$$

or can be simplified assuming an optically dense medium of thickness t with the uniform refractive index n, as given below:

$$\text{OPL} = nt \tag{1.12b}$$

The optical path difference is defined as the difference between the optical path lengths (OPLs). The OPD is an important measure in interferometry, since it is commonly used to find the phase difference between the reference beam and test beam. It is usually defined as follows

$$\text{OPD} = \text{t}(\Delta n) = \frac{\lambda(\Delta\Phi)}{2\pi} \tag{1.13}$$

After measuring the phase difference between interferograms the refractive index can be found using Eq. 1.13. Main principles of interferometry are based on the OPD, phase change and coherence of beams. Two electromagnetic waves are considered to be coherent if their frequencies and waveforms are identical. The optical path between the two beams must be less than the coherence length L_c to produce fringes. The coherence length is based on the center wavelength, λ_c, and the spectral bandwidth $\Delta\lambda$. The coherence time, t_c, is directly related to the coherence length.

$$L_c = \frac{\lambda_c^2}{\Delta\lambda} \tag{1.14a}$$

$$t_c = \frac{L_c}{c} \tag{1.14b}$$

As the OPD approaches zero, the fringe visibility reaches its maximum value. More details of this pehomenon can be found in the SPIE Field Guide by Goodwin [17]. In the design of the interferometer it is important to keep the visibility of the fringes in mind. The interference pattern is created by the superposition of two beams with different amplitudes. The square of the amplitude is known as the beam irradiance, I, which can be measured by a sensor. Each beam is has some phase Φ.

$$I = I_1 + I_2 + 2\sqrt{I_1 I_2} cos(\Phi_1 - \Phi_2) \tag{1.15}$$

The visibility of the fringes can be characterized by the following formula:

$$V = \frac{I_{max} - I_{min}}{I_{max} + I_{min}} \tag{1.16}$$

If V>0.2, fringe visibility is considered to be discernible. There are a number of factors which can influence the visibility in a measured interferogram. As mentioned, a smaller OPD will increase fringe visibility since it improves the contrast against temporal coherence. Spatial coherence also plays a role in fringe visibility. This can be improved by using a spatial filter, such as a pinhole with a focusing lens to remove uncollimated light from the beam. Another important factor affecting fringes is the polarization of the beam. The electric fields can not be completely orthogonal to each other in order for the two beams to interfere. If the two beams have different polarizations, the visibility is related via $cos(\alpha)$, where α is the angle between the two states of polarization. The intensities of the beams can also affect the visibility. For example, as the difference between the beam intensities increases, the visibility approaches 0.2, which leads to indiscernible fringes.

An interferometer itself is a useful tool in metrology, since it can measure small deviations on the order of the wavelength of light used. Depending on the interferometer, accurate measurements can be made at better than 1/1000 of a fringe accuracy. This level of accuracy is typically reserved for phase shifting interferometers (PSIs), where a series of interferograms is created by changing

the phase of one of the interfering beams by some known amount [17]. PIDs require more specialized equipment than what has been used in the following work, but there may be some interest in looking into improving the experimental collection method by creating a single-shot interferometer setup, which can capture these numerous interferograms at once by using a holographic optical element to change the phase in four sections of the camera sensor. This would eliminate noise in data captures due to vibrations.

A single-shot phase interferometer would use orthogonal polarization states in the test and reference beams. After recombining, the holographic optical element is used to create four identical copies of the beam to fall on a image capture. Each of the interferograms passes through a different birefringent phase mask, introducing a phase shift between the test and reference beams at 0, 90, 180, and 270 degrees. Finally, a polarizer with a transmission axis at 45 degrees to the two polarization states is placed after the phase mask so that the two beams interfere. A quarter waveplate is used in this case and would change the orientation of incoming light from P to S or vice versa.

The interferometer in the current work is a homodyne Michelson interferometer that uses a single static image from a camera to capture the phase of two intersecting beams. The design was chosen because it allowed for a simple, cost-effective method to sample interferograms in a living lab space. They are relatively simple to assemble and lead to sensitive measurements of the refractive index. A Michelson interferometer only requires two mirrors and a beamsplitter to operate. A beam expander consisting of two lenses was used to capture a large two dimensional flow region around the test article. An imaging surface was also used to reflect the light at a lower intensity so the high-framerate camera could be protected from any direct pulse bursts. Figure 1.2 shows a diagram of the simple Michelson interferometer with a beam expander upstream.

The experimental set up includes a beamsplitter, which is used to ensure, that light passes through a symmetric medium both on its reflected and transmitted side. This is not a severe issue for inteferometers which use quasi-monochromatic light, since the coherence length for monochromatic light is infinite.

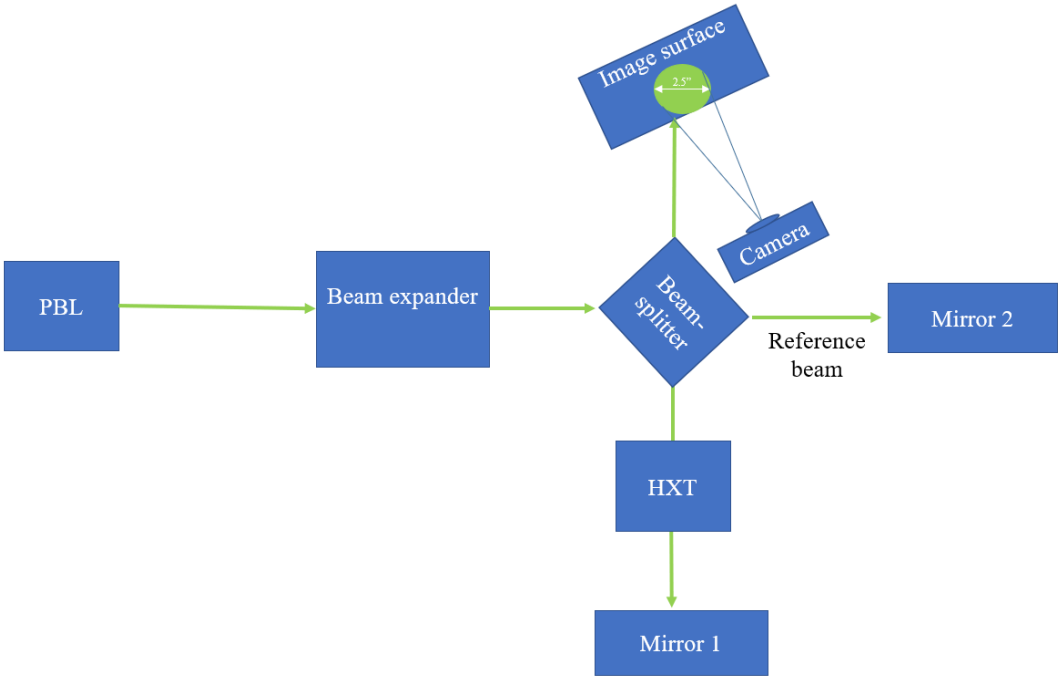

Figure 1.2: Box diagram of generic Michelson interferometer for testing

1.2.2 Description of the Hypervelocity Expansion Tunnel

The subsection briefly touches on the description of the shock tube used in the experiment, since its basic functions are helpful for understanding the experimental set up and operation. The Hypervelocity Expansion Tunnel (HXT), located at the National Aerothermochemistry Laboratory (NAL), was used to create different hypersonic flow conditions. The HXT is composed of three main sections: the driver, the test gas section, and the expansion section. Burst discs and mylar film separate each of these sections from one another until a disc bursts. Figure 1.3 shows the anatomy of HXT, where the red lines represent steel burst discs, and the orange represents a thin mylar film.

A driving gas air (or helium) is used to pressurize the driver section. The pressure is controlled both in the driver section and in the median section between the driver and the test gas. This ensures a larger differential can be reached between the driver and the test gas section. The pressure of the test gas, driver gas, and expansion section gas are changed depending on the desired test conditions

Figure 1.3: HXT Anatomy. Red lines represent metal burst discs while the orange line represents the mylar sheet

for the hypersonic flow. After the expansion section, the gas is free to flow out.

To capture flows at Mach number M=15 and higher a pulse-burst laser and a high-speed camera with 1 MHz frame rate and a 200 nanosecond exposure time were used. Pulse burst lasers can create bursts of laser pulses, which each have a width on the order of 2 nanoseconds. This is a significant adavantage for hypersonic flow testing. For example, a M=15 flow has a velocity of 3,800 m/s or 3.8mm/microsecond. A continuous laser captured by the camera, exposed at 200 nanoseconds per frame, at this velocity will average objects travelling in the flow over a 0.76 mm distance. This means a significant blur will appear while capturing an image with a continuous-wave laser.

1.2.3 Phase measuring algorithms

After collecting the interferograms, the next step is to measure the phase. This proves to be its own challenge, since some interferograms can have hundreds of fringe lines to count and measure the deviations. The classical method of measuring the phase is to visually keep track of the fringe pattern from one image to another and measure how many fringe lines changed between the two images. This approach can only give an estimate of the peak-to-valley change between fringe lines, and this estimate leads to an unquantifiable amount of error in the results. Computational methods can be used to measure the phase and accurately read the interferograms. It is important to collect data with highly visible fringe lines so this does not become an insurmountable issue. The additional benefit to using software is that many interferograms can be averaged, which is particularly important to avoid uncertainties connected with small temperature and flow field fluctuations, which can change the refractive field at any time during camera capture.

Before the analysis of an interferogram, interferograms must be filtered. Work from Qing et al [18] show filtering to be extremely important to ensure the accuracy of the final interferogram. The greatest success found in their work was in using vector filtering. The different filtering methods include non-adaptive filtering, adaptive filtering, and multi-looking filtering. Non-adaptive filtering modifies the original image regardless of its contents. Mean filtering, median filtering, and other methods that consider sections of pixels to average or enhance certain sections of the image are within this category. Adaptive filtering methods filters the original image by enhancing or averaging parts around the vertical/horizontal fringe lines. This is a computationally expensive method, since it requires the image be phase unwrapped before filtering and then rewrapped after filtering. The mulitfiltering method is a more effective method of filtering, but it is heavily affected by noise.

After finding the phase in 2pi modulus, the entire phase map needs to be unwrapped in order to subtract two phase maps from each other properly. There are three main types of phase unwrapping approaches: branch-cut, least square, and other minor methods such as line detection, knowledge intervention, etc [18]. Branch cut algorithms isolate phase error prior to integration by unwrapping the phase choosing only paths of integration leading to self-consistent solutions. The least square method unwraps by minimizing the least square difference between the gradients of the solution and the unwrapped phase. This includes algorithms using Fast Fourier Transform (FFT) and Discrete Cosine Transformation (DCT). The utility of each algorithm depends on the noise present in each interferogram. Certain methods can be more specialized to deal with the noise or aberrations in each captured interferogram.

Postprocessing the interferogram is an intense process due to the numerous sources of error, including noise, discontinuities in the phase map, a violation of the sampling theorem, and invalid data points. There are a number of algorithms that have been developed to analyze interferograms, as shown by Creath and Schmidt in [19]. Each method has its own benefits and retractants. For the static sampled data in the present work, the interferograms were analyzed using Fast Fourier Transform. Spatial unwrapping algorithms require knowledge of a smoothing function after mul-

tiplying the reference and test interferograms together, which was not studied for the current work [20].

After unwrapping the phase of the interferogram, the phase difference between the reference and the test interferograms can be subtracted from each other to find the phase difference plot. In this work, the absolute change in the refractive index can not be found since it was not possible to establish a static reference during testing time. However, the relative difference between different sections of the same captured hypersonic flow can be compared, which still provides a good validation for the theoretical model.

1.3 Overview of relevant work

Thermochemical nonequilibrium effects in a hypersonic flow can be predicted using a semi classical model for the polarizability of diatomic molecules and knowing the species distribution in a hypersonic flow. In this work, the results of a high fidelity Direct Molecular Simulation (DMS) presented by Grover [21] were used. Three different species such as N_2,O_2 and Ar, which together make up all of static air, were studied in detail. The refractive index was calculated using the polarizability concept, so that the results from experiments in the high enthalpy tunnel (HXT) could be compared to the simulated results. The following experimental trials show some of the methods and analysis from HXT experiments.

2. MICHELSON INTERFEROMETER DEVELOPMENTS

This chapter of the thesis documents the effort and learning process required to collect high-quality hypersonic refractive index data. The learning process continues even through the test campaigns, documented in section 3 of this thesis.

2.1 Interferometric Data Evaluation Algorithms (IDEA)

All experiments in the current work collected interferograms which needed to be processed to find the phase change. The phase change was calculated using an FFT-based approach through an existing software developed by TU Graz called Interferometric Data Evaluation Algorithms (IDEA) [22]. The optical path length is the product of the refractive index with the distance travelled. The light experiences a different optical path length before the test and during the test leading to the optical path difference. The purpose of IDEA is to produce a phase change diagram. This phase change can be plugged into a simple OPD equation 1.13, assuming the optical medium observed has a uniform refractive index along its cross section. The phase change$\Delta\Phi$ is the parameter measured with the interferograms. This section documents the method used throughout the testing process to develop the refractive index fields from interferograms.

IDEA works by first taking a FFT of the image file. In order to do this, the image must be padded so that the pixel width and height both satisfy 2^k for any value k. The 2D FFT must then be filtered to mask the symmetrical quadrants of the FFT. This corresponds to any two quadrants that are not adjacent to each other. This restriction is the reason why curved fringes do not work well with the software beyond a certain extent. After filtering the FFT, the chosen frequencies are phase wrapped in a 2π modulus by the software. The resulting image visibly resemble the original image clearly and ideally remove some unnecessary noise. Then a phase diagram is constructed with the chosen phase unwrapping technique: minimum cost matching branchcut method. There are a number of unwrapping techniques, and the different algorithms are designed to preserve an accurate phase map regardless of any discontinuities. This process is done for both the reference

image and the test image. The phase maps are subtracted from each other to create a phase difference plot. The resulting phase difference plot is saved as a .dat file, which is read by MATLAB to find the refractive index field using the OPD equation 1.13. A step-by-step process on how to process data through the IDEA is provided.

1. Open the the reference interferogram written as a .bmp image. It is easier to filter the reference interferogram since there are fewer sharp discontinuities (i.e. no shockwave).

2. Due to the nature of the FFT algorithm the image will need to be padded to have edges of the form 2^k where k is any integer. Figure 2.1 shows the reference image with zero padding. After 2D forward FFT the image will look like Fig.2.2.

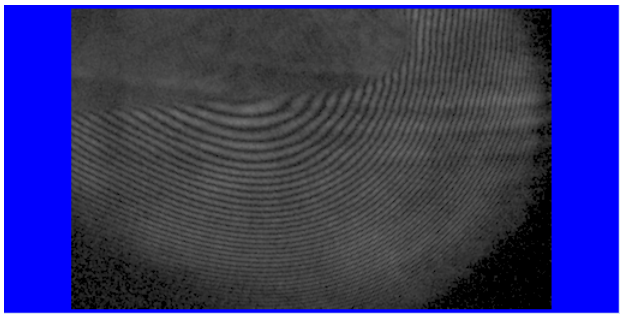

Figure 2.1: Padded image

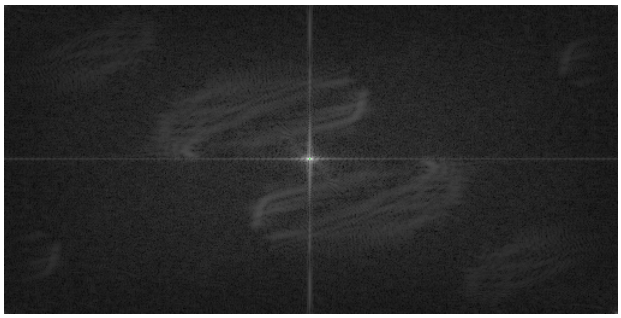

Figure 2.2: 2D FFT

This FFT of an image is the original image translated into the frequency domain. The amplitudes of each frequency are plotted in the x and y directions, with the zero frequency located at the center. Higher frequencies are characteristic of sharp, abrupt lines. The edges of the laser beam shown in 2.1 are represented in frequency space as the bright splotches at the corners of 2.2, due to the abrupt change from light to dark at the edge of the beam. Since the fringes are curved and varying in size, the FFT of this image shows a wide range of higher-amplitude frequency near the zero frequency. The darker regions are typically irrelevant noise. The bright lines spanning from the center off into the horizontal and vertical directions are due to the extremely sharp discontinuities from the padding to the interferogram.

3. This series of steps requires some trial and error to filter out the right amount of the FFT of an image. This phase unwrapping algorithm requires that a maximum of two adjacent quadrants can remain unmasked simultaneously, which is easy to process for good quality fringes.

   (a) Create a mask which covers all except the brighter amplitudes near the center of the FFT.

   (b) After masking out the noise, the fringe pattern should be fairly clear assuming good filtering of the FFT of the image. For instance, figure 2.3 shows an example of a properly-masked FFT and the resulting wrapped phase image.

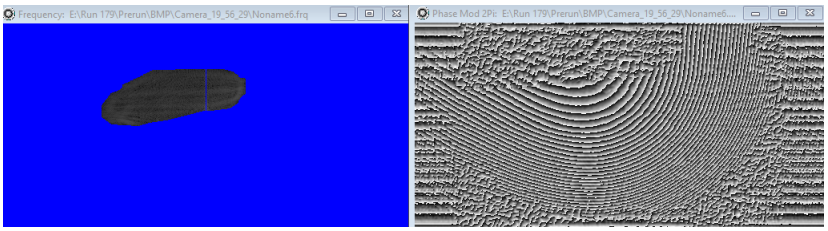

Figure 2.3: FFT (left) and unwrapped phase plot (right)

If the fringe pattern is not clear, some enhancements to the original image must be done as in figure 2.4, which shows the original image compared to its enhanced image.

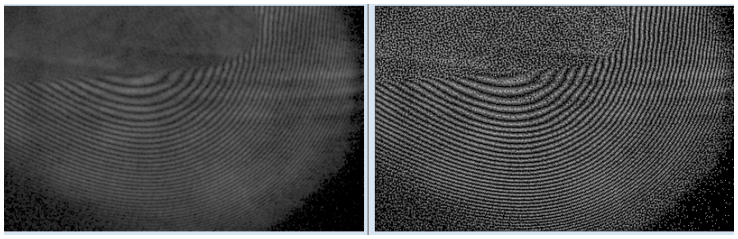

Figure 2.4: Original image (left) and enhanced image (right).

(c) Apply a mask to the unwrapped phase. Refer back to Fig.2.1. The outlying fringes that can not be made out by the eye will also likely not be captured by the computer. At this step it is important to precisely trace the wedge test article boundaries, which helps to establish the shockwave standoff distance in hypersonic experiments. Figure 2.5 shows the mask created for the hypersonic run 179 (conditions for all experimental runs are shown in section 3).

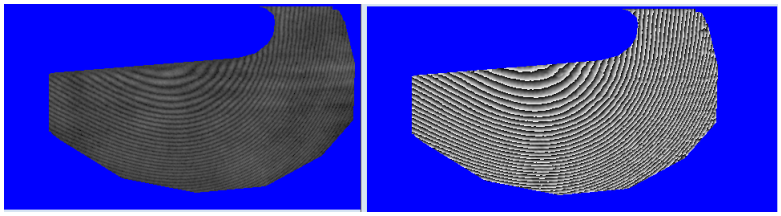

Figure 2.5: Masked fringe pattern applied to original image (left) and unwrapped image (right)

(d) Perform a 2D scan of the wrapped phase to check for any glaring discontinuities in the phase. Any discontinuity should be avoided, but some are unavoidable, particularly at the edges of the image where the fringes are finer. Furthermore, the shockwave introduces abrupt fringe shifts at frequencies that don't occur enough to display a large

amplitude on the FFT of the image. This makes it difficult to discern from the noise. But the minimum cost branchcuts usually stop the discontinuities from spreading further.

Figure 2.6 shows a comparison between properly filtered vs improperly filtered 2D scan of the FFT of the image.

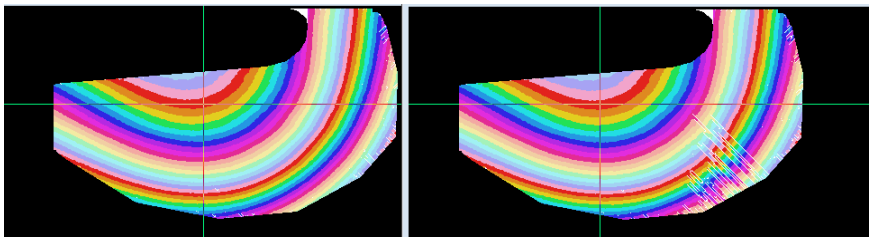

Figure 2.6: 2D scan of the unwrapped phase. A properly-filtered FFT looks like the left image, whereas a poor job was done on the right image.

4. Now that a clean, wrapped phase has been generated, an unwrapped phase difference diagram can finally be constructed after repeating the exact same process with the test image and subtracting both phase diagrams.

2.2 Prototype with PBL0

This section describes how a pulse-burst laser (PBL0) was used to measure phase changes by a Michelson interferometer.

It is important to establish a functional testing device before performing any runs in the Hypervelocity Expansion Tunnel (HXT). A Michelson interferometer was chosen to be the best design option for laboratory experiments based on a number of factors. The only other option that was considered heavily was the Mach-Zehnder setup, which is similar to the Michelson design except that it requires only a single laser pass through the test section. There was interest in capturing a large Field of View (FOV) during hypersonic flow captures so different sections of the flow could be compared to each other in the interferogram. The goal was then arbitrarily set to allow for a

beam size of 4" to be passed through the optical elements. The Michelson interferometer requires the use of only one beamsplitter as opposed to the Mach-Zehnder, which requires the use of two. Furthermore, the Michelson interferometer can be created through a route mainly confined to a single table space. This is important since the exit window of the HXT is relatively small.

After PBL0 was made operational, the first qualitative test was to produce preliminary fringes with the Michelson interferometer design. The original structural plans involved the use of physical test and reference beam arms. A heatgun was applied to one of the interferometer arms to introduce a wavy disturbance across the fringe pattern. The heat gun was assumed to apply a uniform change in the refractive index at a 3" thickness, and the initial refractive index and the wavelength of the light x were assumed ($n_0 = 1$) and ($\lambda = 532$nm), respectively. Figure 2.7 shows a plot of the refractive index for this qualitative test after applying equation 1.13 to the phase change plot.

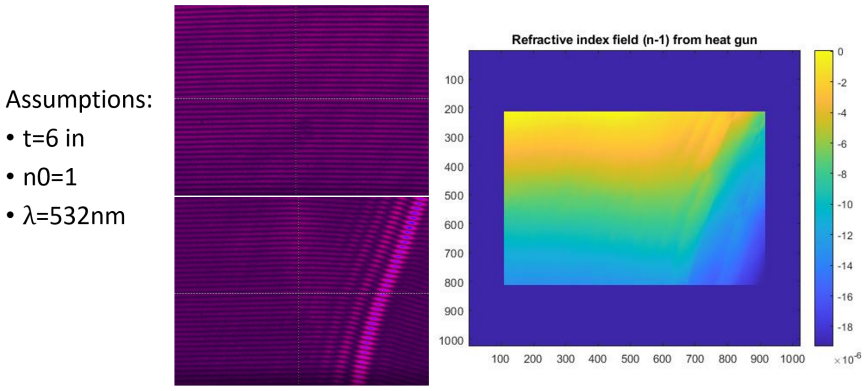

Figure 2.7: Reference and test image on left. Refractive index difference plot on right

The refractive index field ripples with the same ripple generated from the heat gun. It is uncertain how refractive index change along the y-axis was measured. This could be an issue with comparing a separate reference image a test image. Typically, static interferograms can be compared when a certain section of the capture is left undisturbed from the flow. This can not be the case for the hypersonic experiments designed for HXT, since the entire area imaged will be affected by either the freestream or by the effects after the shockwave. Another possible explanation

for this refractive change along the y-axis could be the field actually changed uniformly in that direction due to uneven heating from the heat gun.

2.2.1 Expanded fringe experiment: Acoustic shockwave

The expanded beam was assembled in the same way as the smaller beam, but now larger optical elements were used, including a 6" beamsplitter and a set of 6" mirrors. The output beam was expanded by a 1" diameter +40mm expanding lens and a 8" diameter +380 EFL aspheric collimating lens. The two lenses brought the beam size to 3.25" after expansion. Figure 2.8 shows a box diagram of the interferometer setup.

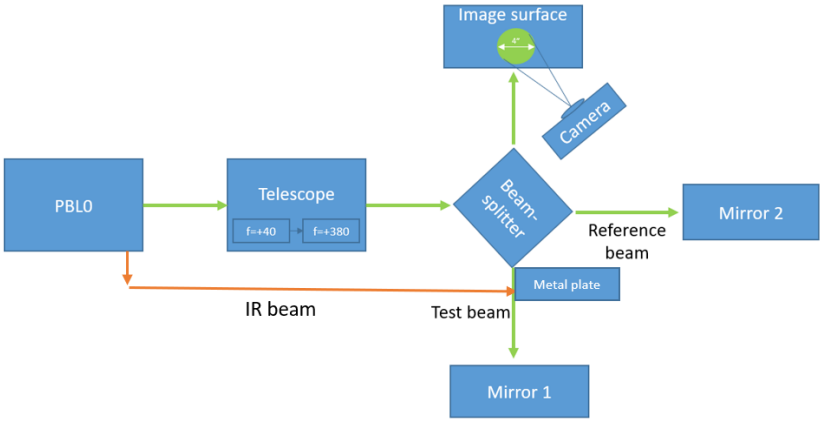

Figure 2.8: Michelson interferometer with PBL0

Notice also in Fig.2.8, there is a separate IR beam picked off from the beam inside of PBL0. This was done to allow capture an acoustic shockwave. The IR beam would generate shockwaves when brought to focus against a metal plate. This shocwkave would occur on the same time scale as the pulse burst capture, and therefore the temporal capture capability of the new camera could be tested as well. The camera used for this experiment was the Shimadzu HPV 2, which was set to the same capture rate as the pulse rate from PBL0, 250kHz. Figure 2.9 shows the physical setup of the metal plate and the lens on the testing arm.

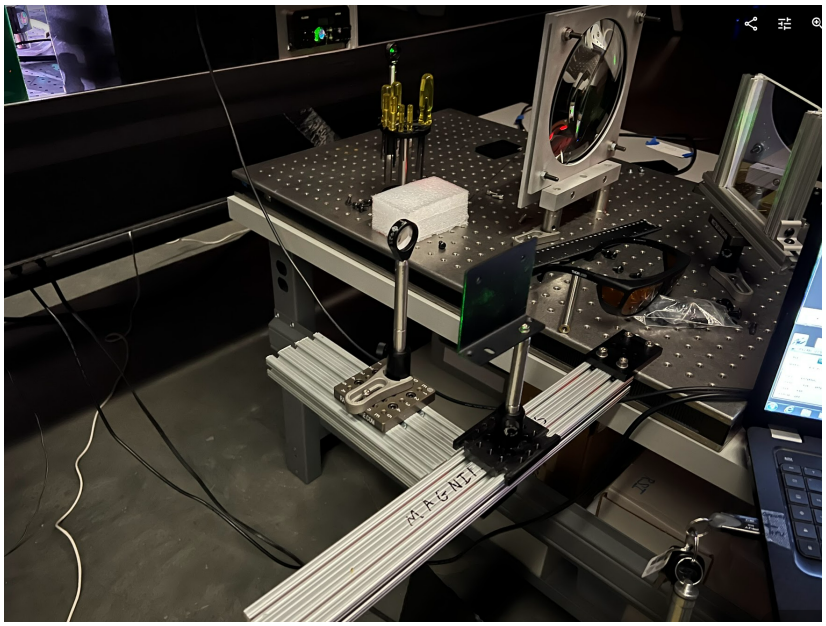

Figure 2.9: Acoustic shockwave test setup

2.2.1.1 Steady-state fringe pattern exploration

Figure 2.10 shows a fringe pattern generated by the interference of these two expanded beams.

Two sets of curved fringe patterns seem to exist, which is due to the same aberrations present in Fig. 2.10. Figure 2.11 shows the real image and the image of the generated 2D scan, which shows 75 fringes.

An acoustic shockwave was generated via a focused IR beam on a metal plate. Figure 2.12 shows the acoustic shockwave data frames. It is seen, that the shockwave expands, but it is too small to observe any significant impact on the fringe pattern and phase change. Summarising all efforts above, a postprocessing technique was developed and shown to work.

2.3 Pretest considerations

This section shows the preparations that were considered prior to the test campaign to ensure smooth operation and adequate data collection.

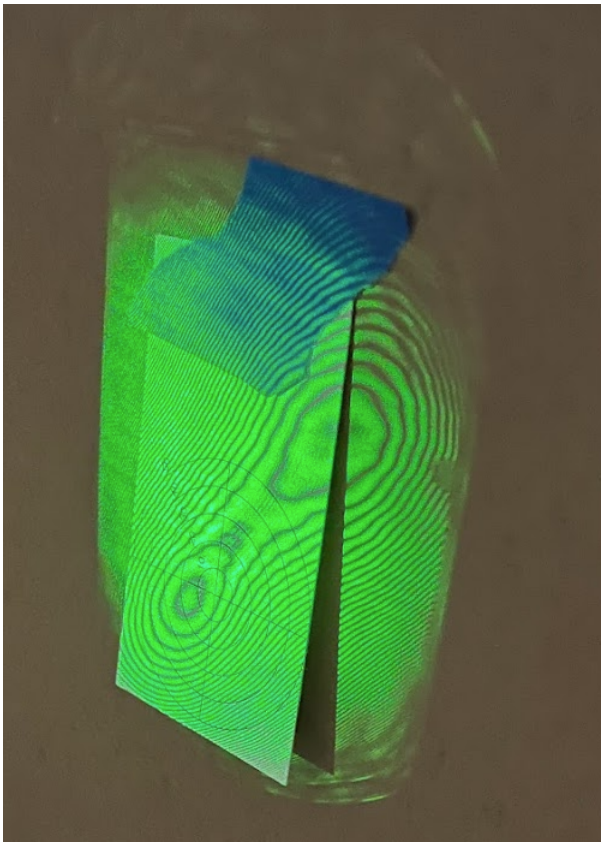

Figure 2.10: Fringe pattern from 3.25" beam

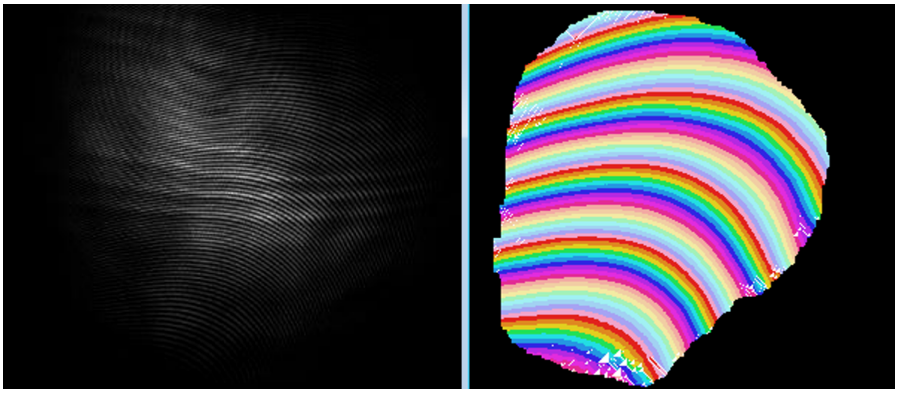

Figure 2.11: Real image on left. IDEA 2D scan on right.

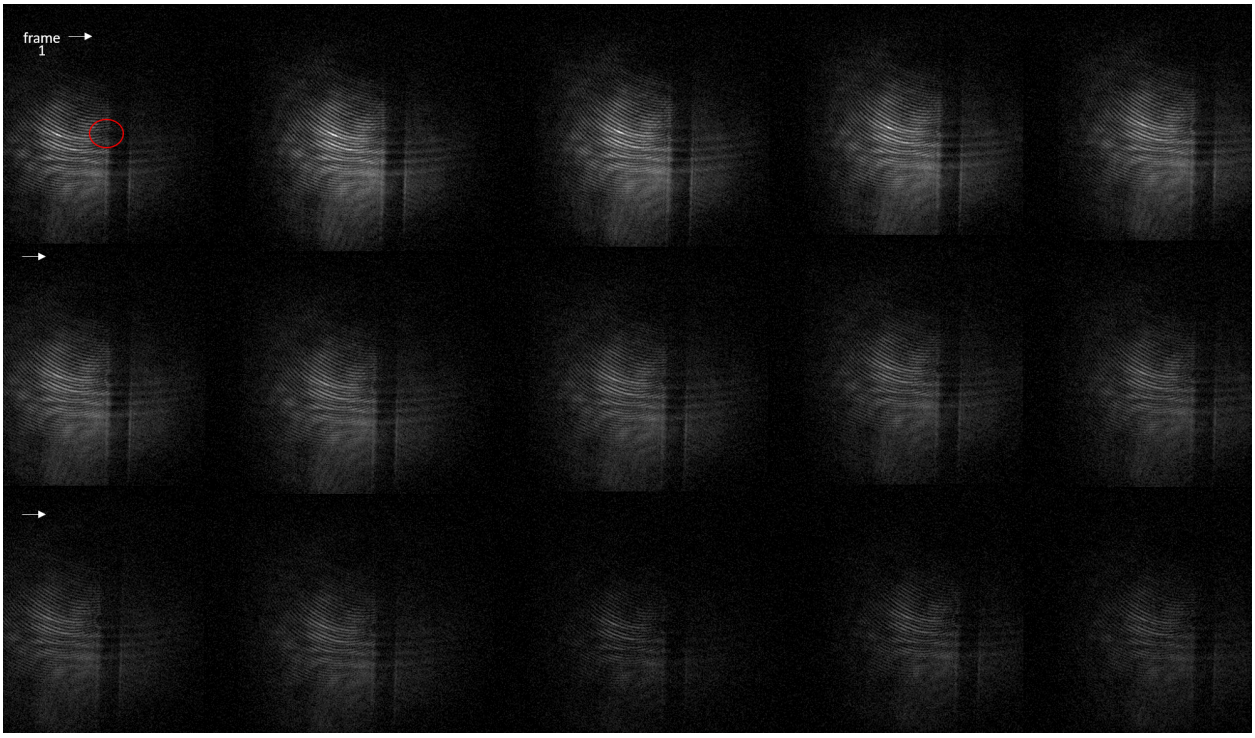

Figure 2.12: Frame captures from Acoustic shockwave. Relative location of shockwave is circled in red on first frame

2.3.1 Camera lens choice and working distances

It is important to match the camera Field of View (FOV) to be the desired size, which should be smaller than the expanded beam size so as many pixels of the high-speed camera can be used as possible. The Shimadzu HPV-X2, used in each of the test campaigns, has a resolution of 400x250 pixels, each with a 32 micron pixel size. The resolution becomes a limiting factor to determining the phase change across a certain region with good accuracy.

Another question was a choice of lenses, which depends on three parameters such as the working distance, the field of view and the focusing range. The working distance (WD) is defined as the distance from the first optical element to the object. The field of view (FOV) is the size of the viewed object in real space. There are two types of lenses commonly used for cameras: a fixed focus lens and a fixed focal length lens [23]. A fixed focus lens is designed for a single working distance. Though they typically have better optical clarity than fixed focal length lenses, they can

not be adjusted for different working distances. A fixed focal length lens can be used for different working distances through a variable zoom. The limits of this zoom is defined by the free working distance, which is the range of working distances acceptable for the lens. Another important specification is the focusing range, which is the range of distances the lens can operate, starting from the image plane.

The field of view can be calculated as a function of the working distance by using formulas from paraxial optics [24]. The lens equation relates the focal length of a fixed focal length lens to the object distance z and image distance z'.

$$\frac{1}{f} = \frac{1}{z} + \frac{1}{z'} \tag{2.1}$$

The FOV is the desired object size, and the sensor size is the desired image size. The magnification of the image is defined as the ratio of the object size to the image size.

$$m = \frac{H}{H'} = \frac{z}{z'} \tag{2.2}$$

Rearranging the two equations leads to a relationship between the object distance z, now referred to as the working distance, and the focal length of the lens, given a sensor size H' and a desired FOV H. This equation is crucial to ensuring the desired FOV is attainable.

$$H = H'(\frac{z}{f} - 1) \tag{2.3}$$

Equation 2.3 does not include limits to the practical working distances allowed by the lens, which can be found in the specifications of the lens itself, referred to as the free working distance. It should be noted that equation 2.3 was derived using paraxial approximation, so working distances closer to the extremes may lose accuracy between the predicted and observed FOV.

2.3.2 Development of the optical set up for experiments in HXT

The ideal beam profile for interferoemtry is a flat top distribution. An unequal amount of lighting at the edges, as is common with a gaussian distribution, can lead to errors and difficulty in postprocessing the interferograms. An issue with flat top distributions is that it quickly devolves into airy-disc distributions after passing some distance. The airy disc further devolves into a gaussian distribution after some greater distance away. To adjust for this, a relay system was used to preserve the quality of the beam and avoid some of the devolution into a Gaussian pattern. Because a flat top distribution is difficult to create in the first place, it leads to issues in postprocessing the beam.

The beam profile measured at the image plane is also affected by the scattered light from HXT windows. This issue is resolved by carefully blocking the beam during different stages of aligning the test arm. Other components of the optical system include two 4" Thorlabs dieletric broadband mirrors (BB4-E02), which have a surface quality of $\frac{\lambda}{10}$. Additionally, a custom fused silica beamsplitter with 50%±4% reflectivity for 532nm light at a 45 degree angle, designed for P-polarized light (CVI Laser Optics BS1-532-50-2025-45P) was used. The beam expander is composed of two lenses. The expanding lens is a 1" f=30mm plano convex lens. The collimating lens is an 8" aspheric lens EFL=+380mm (Ross Optical L-PCX348/110). Figure 2.13 shows a typical interferometer setup adjacent to HXT.

2.4 Grate Alignment method

Many hypersonic tests measuring the refractive index utilize a Mach-Zehnder design since it does not run into any issues with retracing the beam back through the test section. This proved to be a difficult issue to solve, but over the course of numerous experiments, a technique was developed to verify not only that the beam is returning at exactly the same path as going in, but also that the beam itself is as close to perfectly collimated as possible. It is important particularly for the Michelson interferometer experiments because the resolution of the phase change data is improved with better retracing of the original path. This ensures the same path is crossed by the beam when

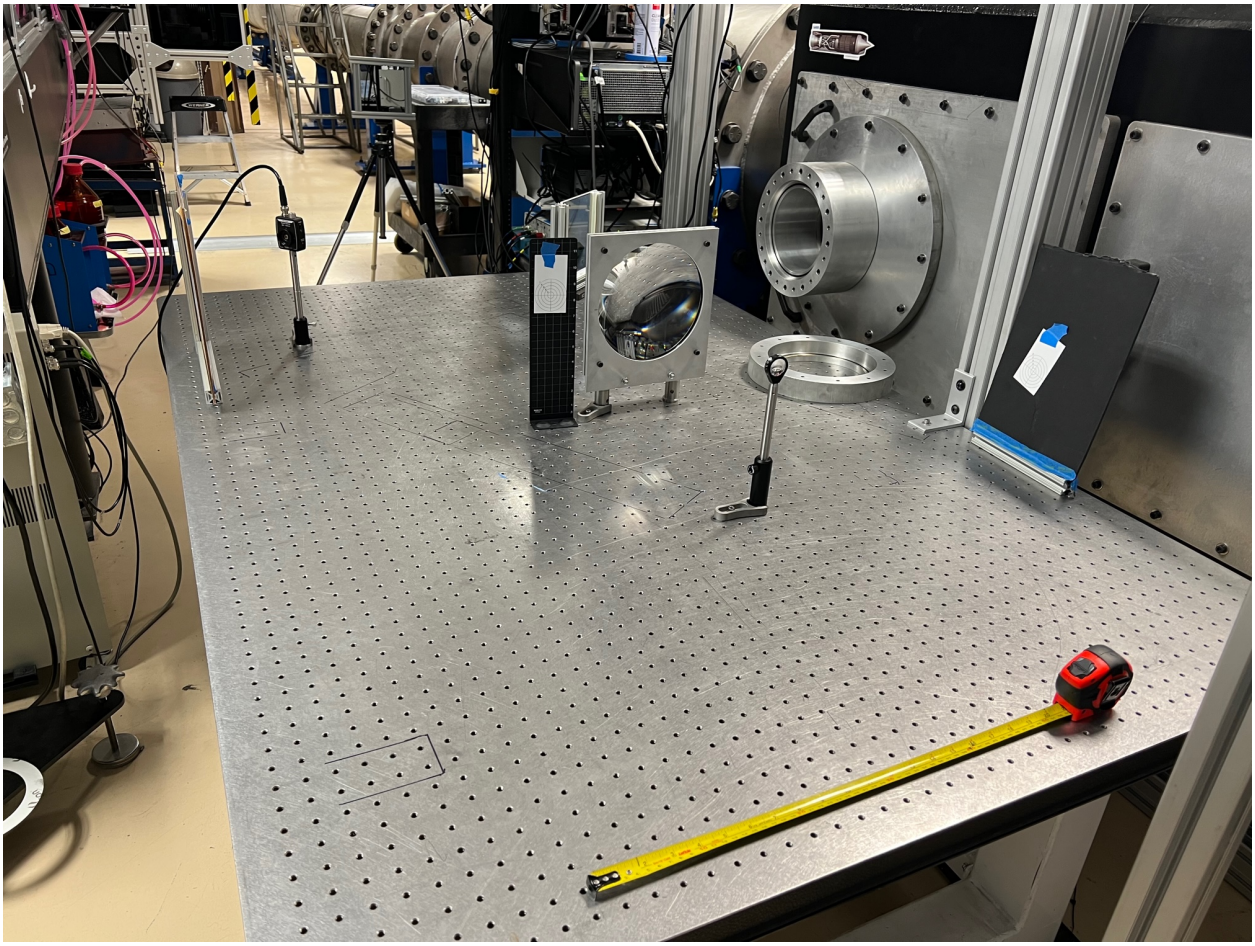

Figure 2.13: Generic HXT table setup for interferometry

passing through the tunnel at the same size. The method works by using a grate (Fig. 2.14) to block a portion of the beam throughout the field of view. The grate is necessary, as opposed to just using a single thin wire, because the collimation can also steer the return beam outwards if the beam is diverging or inwards if it is converging. Figure 2.15 shows how the alignment method works to correct for both collimation errors and retracing errors.

2.5 Summary of Developments

This section shows the development of the interferometer and measurement techniques and set up required to analyze the data collected during experiments. An extensive review of interferograms analysis using IDEA software was provided. A description of the interferometer devel-

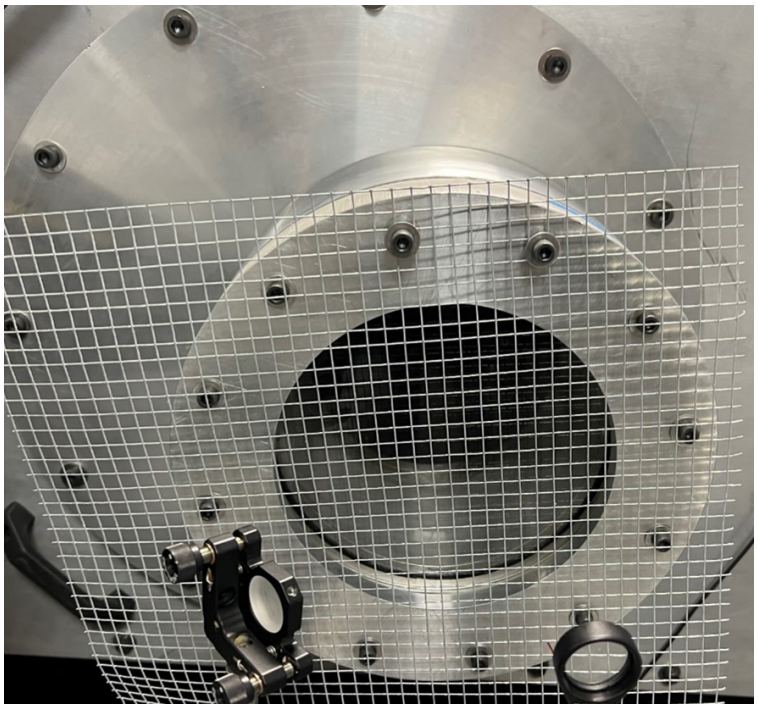

Figure 2.14: Grate in front of window

opment from its prototype stage was given to provide the basis for the start of HXT experiments. Analysis of the desired FOV, the beam quality, lens characteristics and grate alignment method was also provided in this section. It was shown that the developed grate alignment method decreases the amount of potential error sources from experiment.

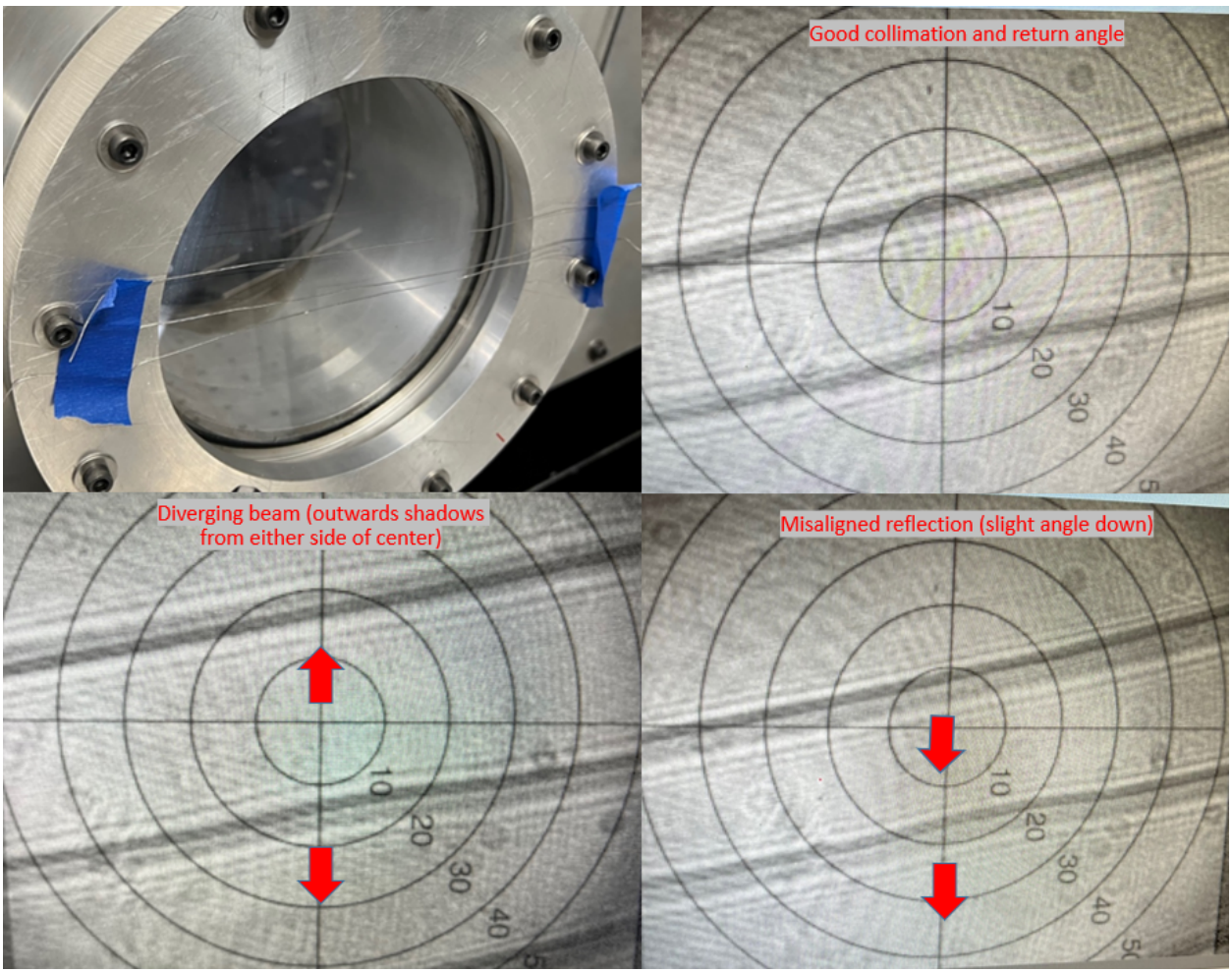

Figure 2.15: Collage of pictures showing examples of a beam with improper collimation, another with improper retrace angle, and another that is well-collimated and retraced

3. HYPERSONIC EXPERIMENTS AND SIMULATIONS

This chapter presents the data collected from HXT experiments. A comparison is made between the collected data samples and the theoretical model. An important thing is that the HXT itself is new, and there is still more to be discovered about how it operates. Over the course of three test campaigns, 22 runs were conducted, which is over 10% of HXT lifetime.

3.1 HXT Test Campaign 1

Test campaign 1 was the first time refractive index data was collected from HXT. This campaign served as a validation that refractive data could be collected from the shock tube. The HXT was used to perform four refractive index flow studies, referred to by their chronological order as HXT runs 140-143. at the conditions listed in Table 3.1.

	Run 140	Run 141	Run 142	Run 143
M	8.5	FAIL	8.5	8.5
Re $[1 \times 10^6]$	9.6	FAIL	0.2	1.3
T [K]	250	FAIL	660	460
$\rho\,[1 \times 10^{-3}\,\frac{kg}{m^3}]$	56	FAIL	14	8.5

Table 3.1: Actual run conditions for test campaign

A double wedge test article was used to generate a set of oblique shockwaves, which formed some distance downstream into a normal shockwave, refferred to as a Mach stem. Despite the fact that the Mach stem was captured in run 140, the optical density was too great and distorted any useful information from the stem. Run 142 also captured the mach stem, but the optical density was instead extremely weak, so it was difficult to analyze the data. The viewing angle from this experiment also proved to be a challenge in postprocessing. especially when the camera did not successfully capture the entire shockwave. Low contrast fringes also make it difficult to postprocess the data.

Figure 3.1 shows a block diagram with geometric measurements of the HXT test section. The laser passes through HXT at a viewing angle with a large amount of uncertainty. Therefore, the most conservative estimate for the viewing angle was determined using the geometric constraints of the HXT window and the size of the laser: so 3.7+-3.2 degrees is the viewing angle for these HXT runs.

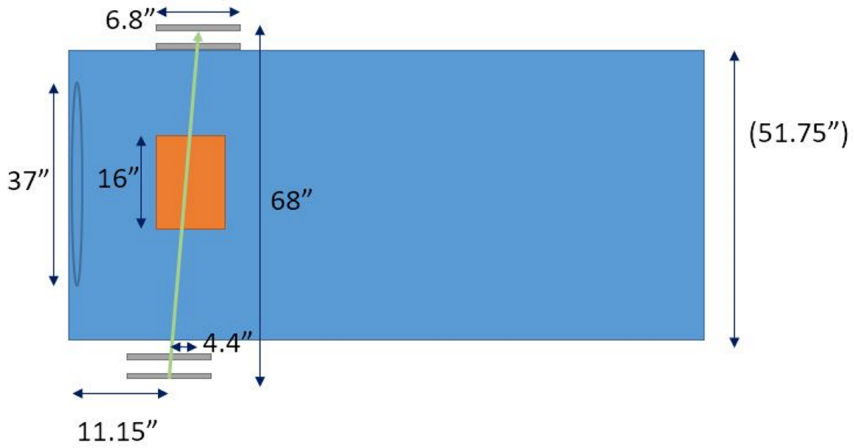

Figure 3.1: HXT block diagram with laser angle overlaid

Figure 3.2 shows the double wedge test article used in this campaign.

3.1.1 Run 140 capture and post-processing

Figure 3.3 shows a reference image and a test image of the run.

Regardless of the fringe visibility, the Mach stem was too dense to possibly track any fringe through the shockwave. In addition, the reference image had fringes that were too weak to be properly identified and tracked via IDEA. Figure 3.4 shows the 2D scan from IDEA, which does not sure any lines without discontinuity, thus this capture was not useful for analysis.

Run 141 failed due to a leak occurred and contaminated the pure nitrogen test gas with a significant amount of Oxygen. Thus, exact conditions of this run are unknown. Figure 3.5 shows the run data, where the mach stem is circled in blue.

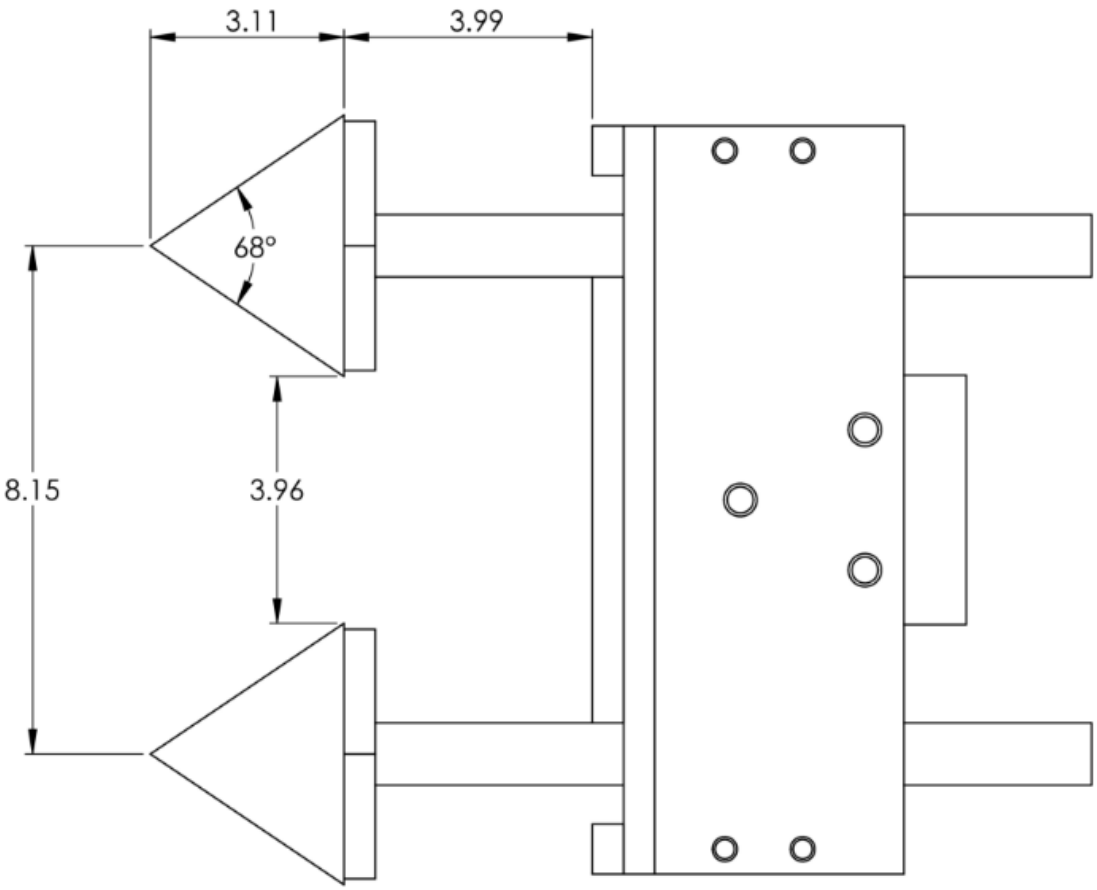

Figure 3.2: Test Campaign 1 double wedge test article

3.1.2 Run 142 capture and post-processing

The system was realigned to capture high-contrast interferograms. The Mach stem was captured in this run, but it was not very strong or visible. Figure 3.6 shows the data capture from the run.

The shockwave is almost completely invisible, but the phase difference was successfully tracked. Figure 3.7 shows the calculated refractive index field for this flow, assuming a uniform optical density over 16" (which is the span of the double wedge test article).

The Mach stem is shown by the refractive index change across the x-axis, while the reflected shock produced from the Mach stem formation is shown by the refractive index change across the y-axis. The oblique shockwave leading to the formation of the Mach stem is not apparent in the

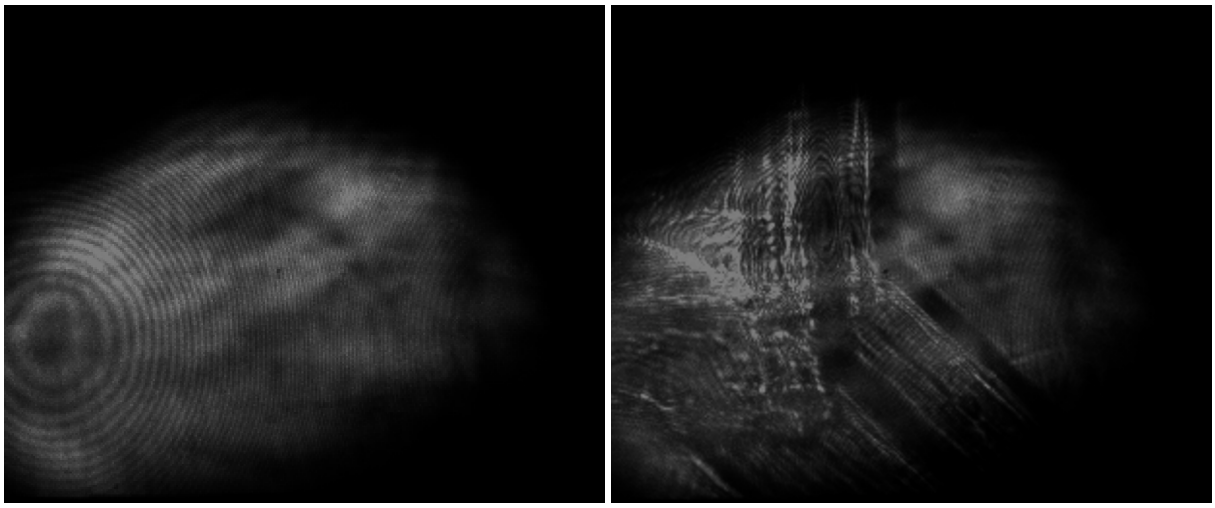

(a) Reference (b) Test

Figure 3.3: Run 140 image captures

Figure 3.4: Run 140 Original image, then enhanced, then analyzed with IDEA

dataset, likely because it is too faint for observation. The thickness of the shockwave can also be seen to span approximately 15mm, or from the 20mm mark to the 35mm mark in Fig. 3.7. The refractive index changes linearly over that region, which indicates a uniform refractive field. Assuming this uniform change in the refractive index occurs over the span of the test article, and also assuming there is no retracing error when returning the beam through the HXT, the viewing angle is calculated to be 2.1 degrees. This is within the viewing angle uncertainty mentioned earlier.

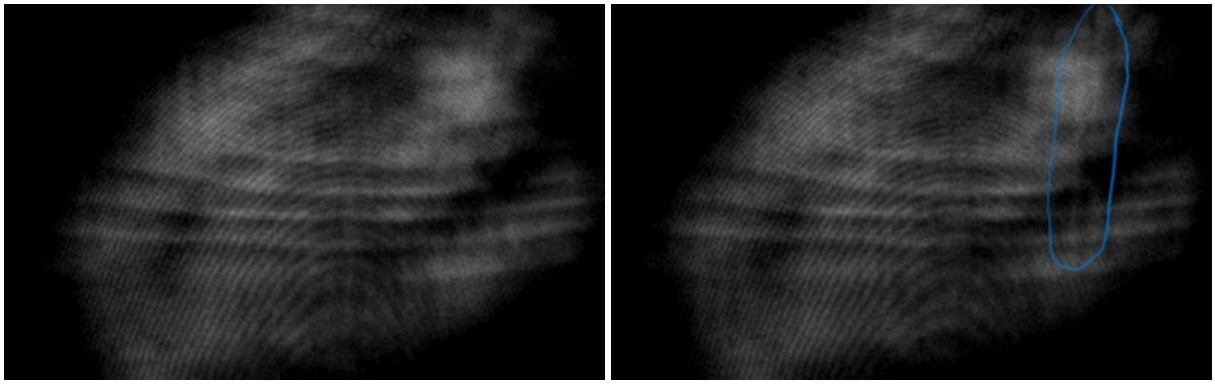

(a) Reference (b) Test

Figure 3.5: Run 141 image captures

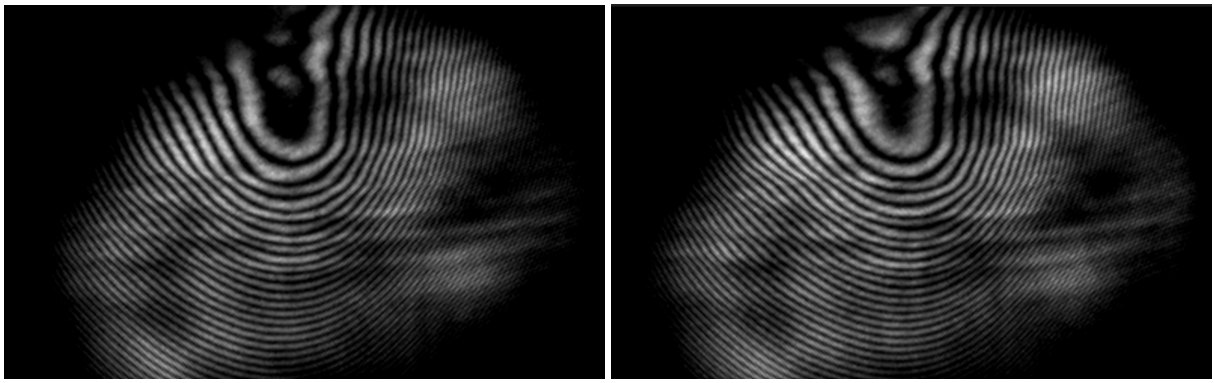

(a) Reference (b) Test

Figure 3.6: Run 142 image captures

3.1.3 Run 143: capture and post-processing

The capture was approximately 95mm away from the nose of the test article. The oblique shockwave was captured. The reference fringe pattern was setup to be as linear as possible. Figure 3.8 shows the data collected from this run.

Because only the very edge of the interferogram captured the Mach stem, it was impossible to analyze the phase change across it. The free-stream and the oblique shock wave were analyzed for the refractive index change. Figure 3.9 shows the experimental refractive index field created using the reference and test image. The predicted plot is also included as a reference. The order of

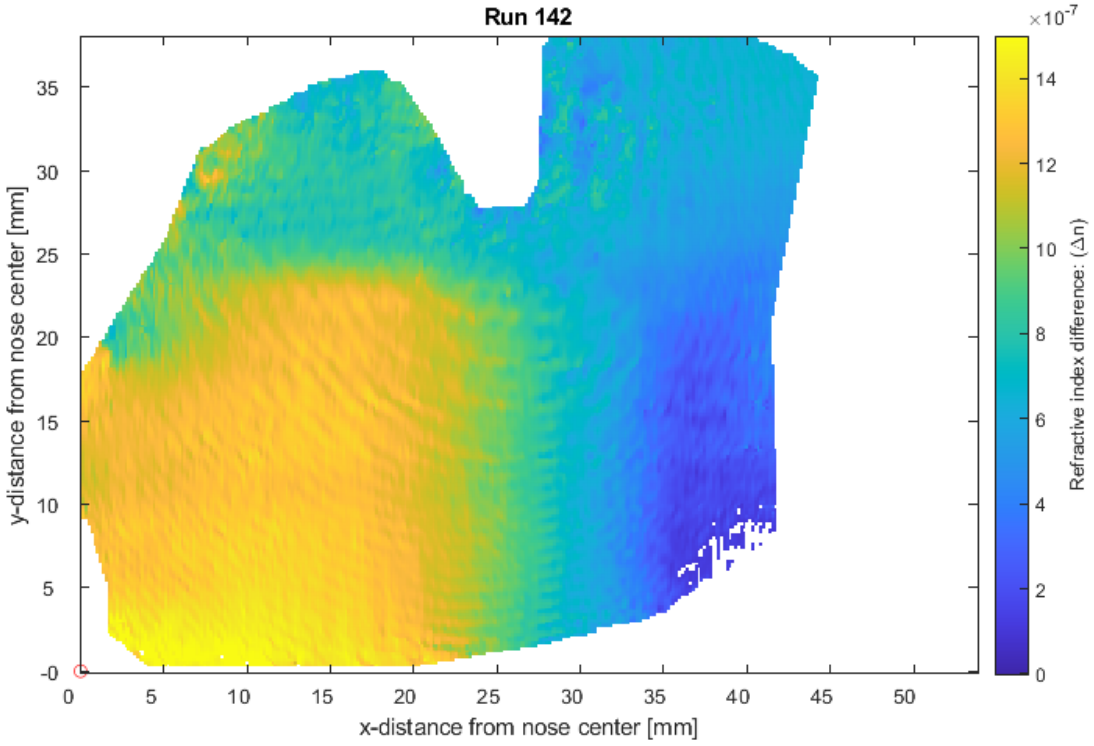

Figure 3.7: Run 142 Refractive field

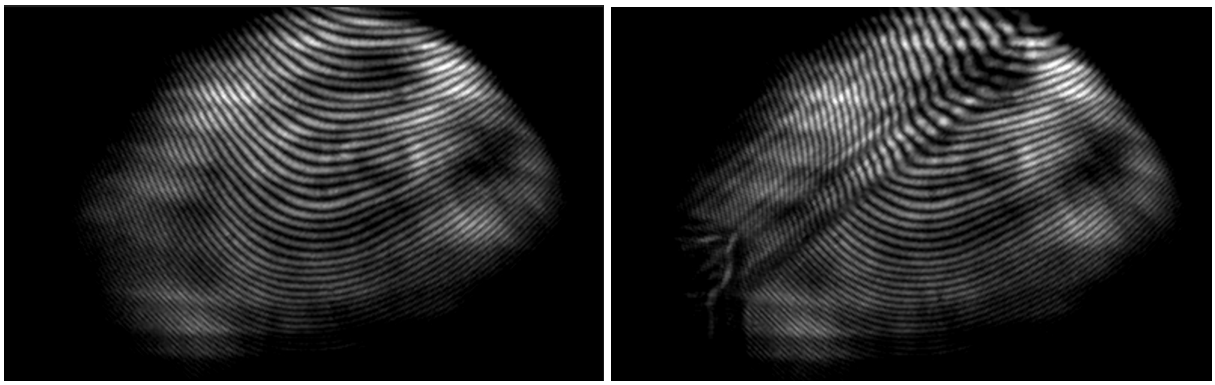

(a) Reference (b) Test

Figure 3.8: Run 143 image captures

magnitude matches the refractive index measured across the oblique shock wave.

The results from this experimental campaign showed that the developed experimental set up works for high enthalpy flows. Furthermore, data analysis shows that the refractive index could be

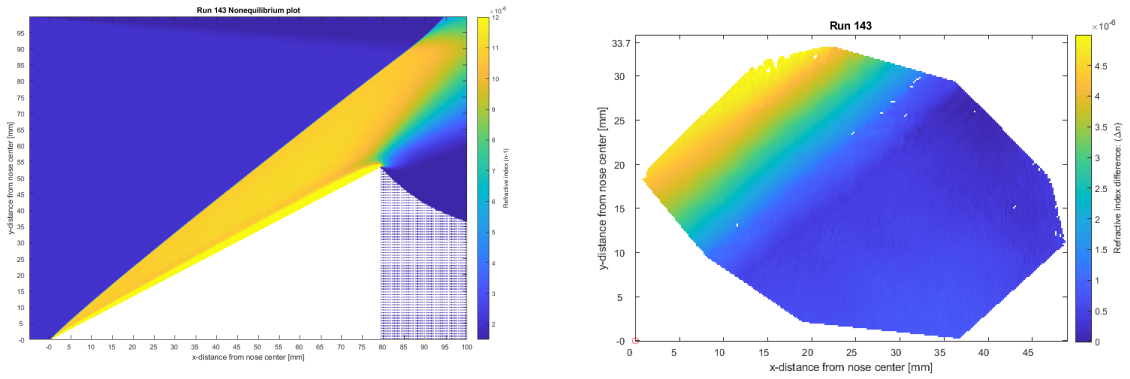

(a) Predicted (b) Measured

Figure 3.9: Run 143 predicted vs measured refractive field

measured in these high speed conditions. But the Mach stem was difficult to capture, since varying run conditions changes the location of the Mach stem. This means it was difficult to extract useful data. The solution to this problem was to design a blunt body wedge, which would reliably generate regions of nonequilibrium flow behind a predictable shock wave.

3.2 Test Campaign 2: blunt wedge pure nitrogen flow

This test campaign collects more data at high a high Mach number and enthalpy. These conditions correspond to high level of vibrational nonequilibrium in a hypersonic flow, which could potentially be measured in experiment to help validate the model. A blunt-body wedge at 7-degree half angle shown in Fig. 3.10 was designed to control the shock wave location. A disadvantage of this test article is that a portion of the flow is obstructed by the test article itself.

The test campaign involved using nitrogen as a test gas at Mach number M=8.5. Six test runs were performed, referred to by their chronological order as HXT runs 174-179. Table 3.2 shows the successful run conditions for these tests compared to the condition that was used as a target.

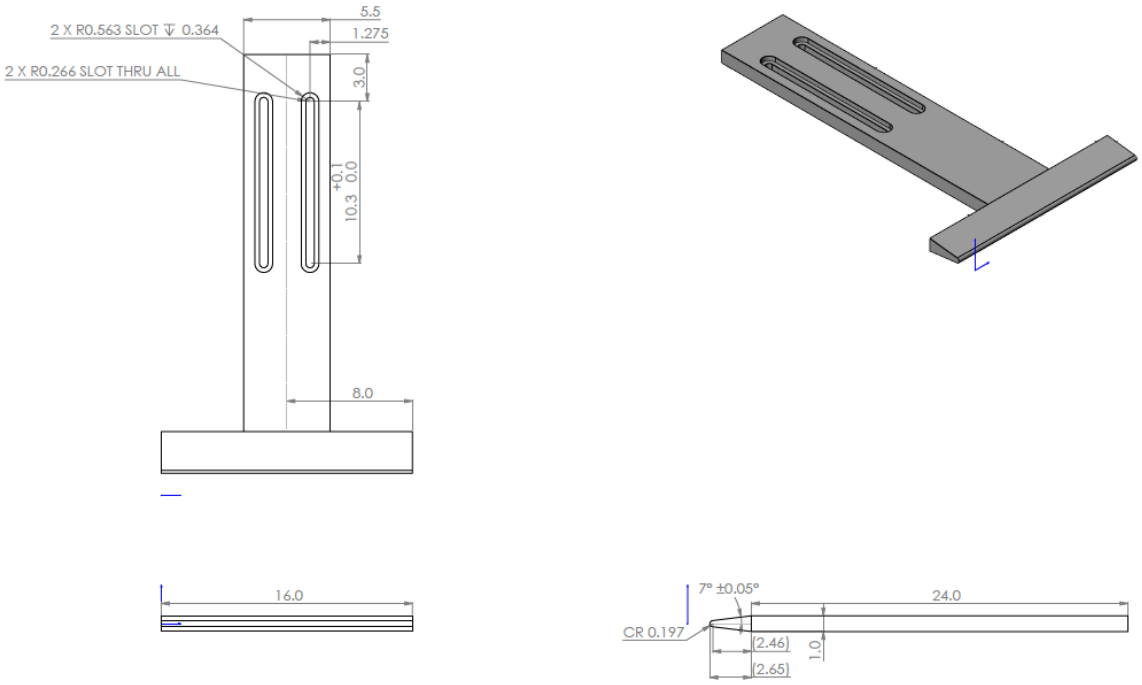

Figure 3.10: Wedge test article

	Targeted	Run 178	Run 179
M	8.7	8.57	8.75
Re $[1 \times 10^6]$	0.177	0.165	0.179
T [K]	216.8	223.0	214.5
$\rho\ [1 \times 10^{-3}\ \frac{kg}{m^3}]$	0.96	0.92	0.97

Table 3.2: Test campaign 2 run conditions

3.2.1 Run 178 capture and post-processing

Figure 3.11 shows the images captured. There was very little difference in the test image over time, which indicates a steady run condition. The oblique shockwave can be clearly seen in the image, but the discontinuity is less pronounced closer to the nose of the nose of the test article. This is because the shock wave is curving in the same shape as the fringe pattern closer to the nose, which leaves less of a visible impression on the phase. Table 3.2 shows the run conditions measured from the experiment, which is fairly close to the desired run condition.

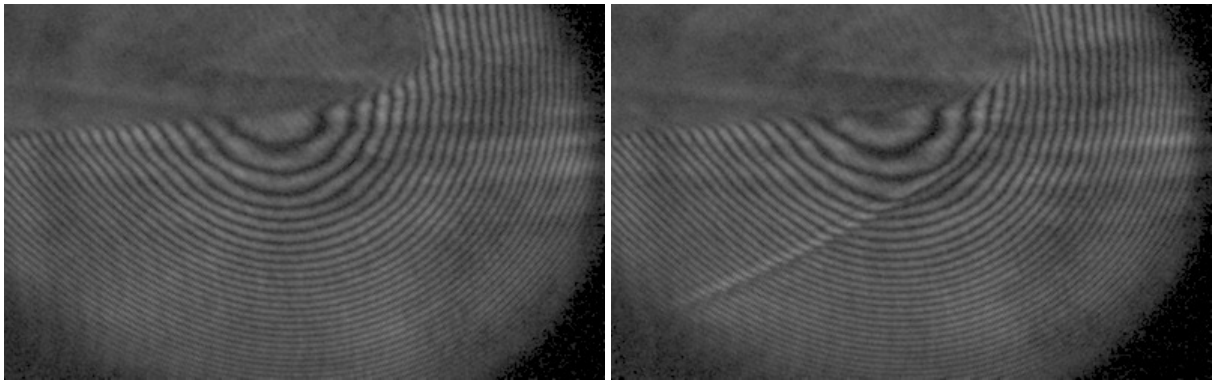

(a) Reference (b) Test

Figure 3.11: Run 178 image captures

The data collected from Run 178 was more difficult to analyze than Run 179 since it exhibited a larger curvature. The restrictions of the FFT algorithm do not allow for fringes to have a significant x-direction frequency and y-direction frequency simultaneously. A 2D FFT transform does not allow phase unwrapping if locations in quadrants symmetric to the origin are left unmasked, which poses a big issue if a fringe pattern is exhibited with some frequency both along the x axis and y axis. Important information is forced to be cut off, which leads to discontinuities in the unwrapped phase. Figure 3.12 shows an example of an attempt to analyze Run 178 in one piece. There is a sharp discontinuity on the x-axis since the chosen FFT mask allowed for information from the top two quadrants only.

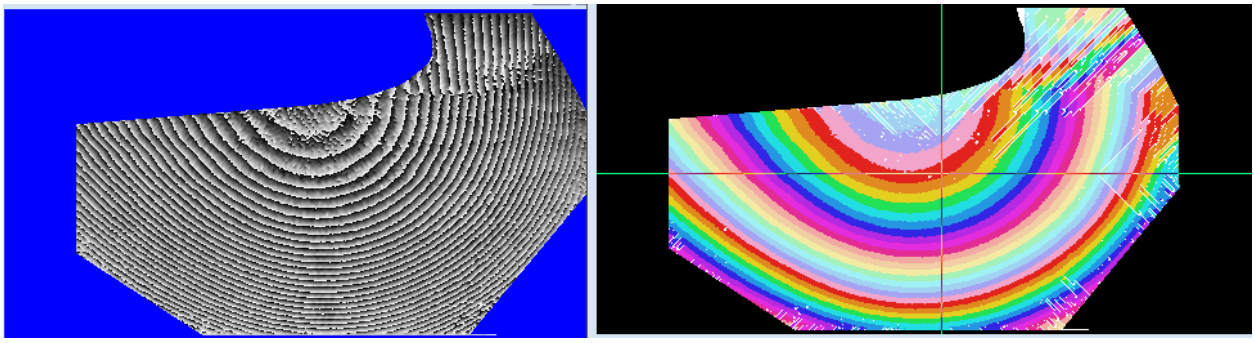

Figure 3.12: Run 178 postprocess in one image. Wrapped phase on left and 2D scan on right

To avoid the discontinuities, the reference image and the test image were taken in congruent pieces. Figure 3.13 shows the process taken for the reference image. The top row shows the original image and the enhanced image (a local enhancement on 3x3 kernals was used at a strength of 0.5). The next row shows first the section of the FFT chosen for the phase unwrapping. This allows for the vertical fringes to be unwrapped without discontinuities, as shown in the following image. The final image is the resulting phase diagram after applying the minimum cost branchcut method. The final row is the same process applied to the top section of the FFT. Note that since this was taken into two pieces, it was important to find a common reference pixel to set $\Phi = 0$. The pixel (285,225) was chosen to be zero for both images, since it is a shared pixel between both images.

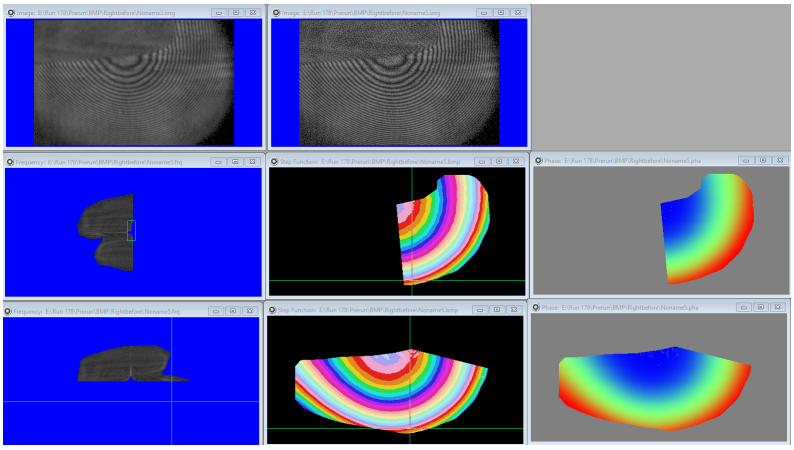

Figure 3.13: Run 178 IDEA reference phase plot development process

This same process was applied to the test image to find the the phase differences and refractivity differences. Figure 3.14 shows the different ways the total phase difference plot could be constructed.

Figure 3.14 is comforting because it shows the phase difference plots could be combined after being processed separately without any effect on the phase different plot. It is difficult to even see the difference between the body-filled and nose-filled phase plots, but close inspection reveals a

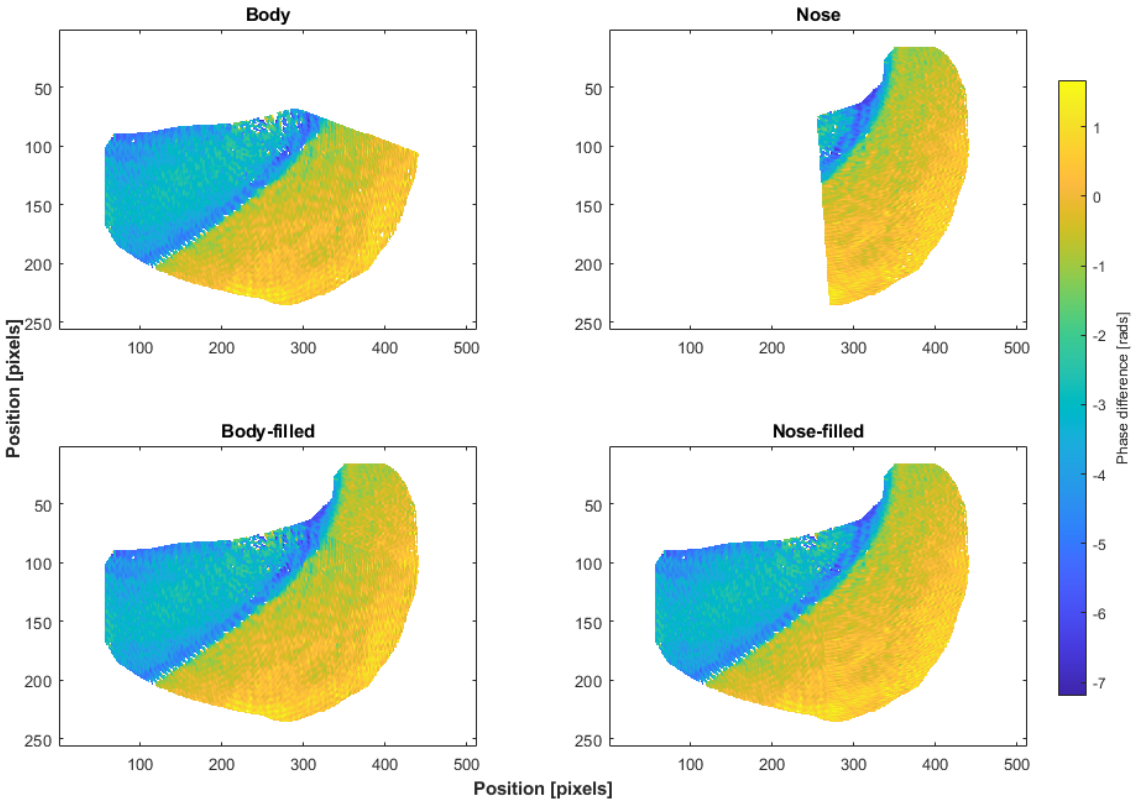

Figure 3.14: Run 178: constructing full phase difference plot

small discontinuity at the interface between the nose or the body fill-in. This discontinuity is less significant than experimental noise, which will be discussed in the following chapter.

Using measurements taken from the experiment, a scale can be established per pixel, which allows for a direct comparison between experimentally-collected refractive values and the theoretically-predicted refractive values. From the phase difference plots the refractive field can now be constructed and compared to experiments. Figure 3.15 shows the predicted refractive index field and the experimental refractive index field.

It should be noted that the refractive index values from the theoretical plot are absolute refractive index values, while the refractive index values from the experimental plot are relative. Thus the minimum value for the refractive field is 2e-7 for the theoretical plot, compared to the minimum value being set to zero for the experimental plot. Since there is no undisturbed reference

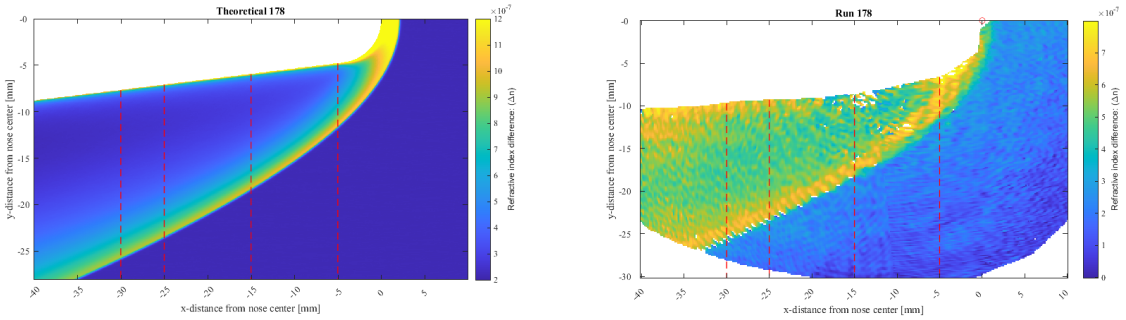

(a) Predicted (b) Measured

Figure 3.15: Run 178 refractive fields: predicted vs measured

area within the interferogram, the absolute phase difference can not be extracted from collected data. But analysis of the difference between the experimental and theoretical data sets can be done by taking cross sections from each plot. These cross sections from each data set are marked by red dashed lines in Fig. 3.15. Values from the experimental data set were interpolated to compare directly to the theoretical data set, which has a much higher resolution. All values from the experimental data set were shifted by the freestream refractive value in the predicted data set for a direct comparison. Figure 3.16 shows how the measured refractive field compares to the predicted field at various cross-sections of the flow. The percent difference is overlaid on the plot, treating the nonequilibrium predicted values as true values. The percent difference between nonequilibrium and equilibrium calculations is also overlaid on the plot, since the amount varies depending on location on the wedge.

The percent difference caused by nonequilibrium effects are close to 0%, reflecting the fact that pure nitrogen represents a thermally frozen flow at this enthalpy. Chemical nonequilibrium and appearance of atomic nitrogen due to dissociation reactions has a bigger influence on the results. The important thing to note is that the maximum refractive values are fairly close to what is predicted from experiments. But the percent difference at some points in the flow is actually fairly high. This is due to an experimental error and uncertainty of the measured data, which will be analyzed the following section.

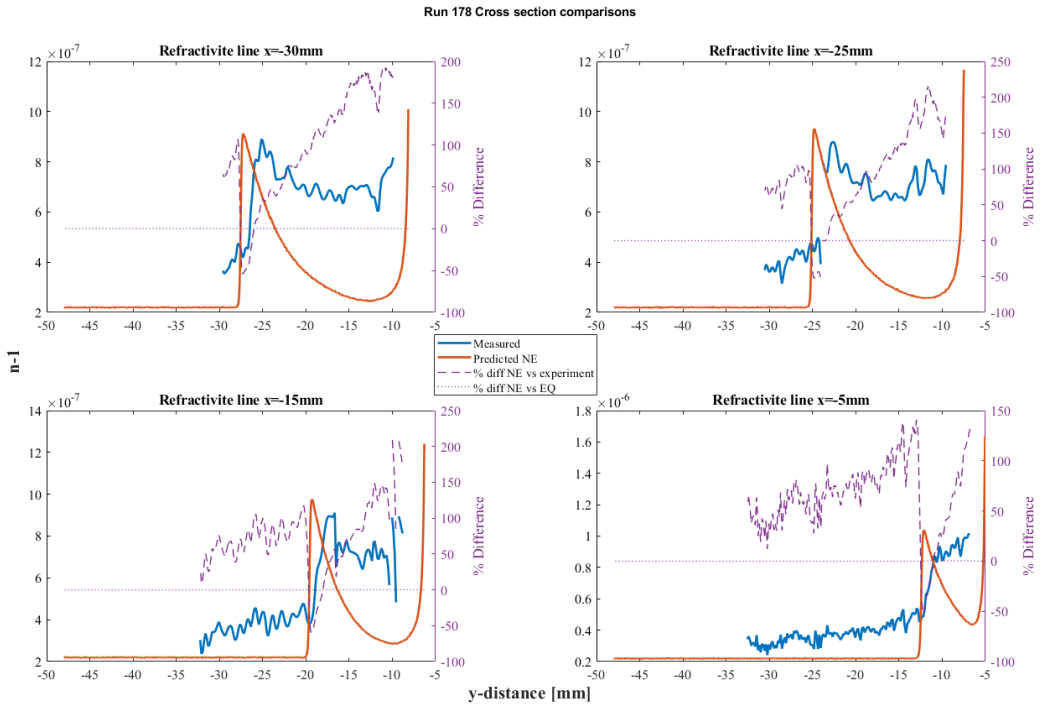

Figure 3.16: Run 178: Refractive index comparison

3.2.2 Run 179 capture and post-processing

Table 3.2 shows the conditions of this run, which are almost perfectly matched with the desired run conditions. Figure 3.17 shows the images captured for the test. The shock wave was almost perfectly still during the entirety of the test capture time, which lasted about 1 millisecond.

The phase difference plot was generated in one piece using IDEA, and the refractive index field was calculated at every point in the flow. Like Run 178, cross sections from each data set are marked by red dashed lines in Fig. 3.18. The minimum value of the experimental refractive field was set to the minimum value of the theoretical plot for comparison. Figure 3.19 shows how the measured refractive field compares to the predicted field at various cross-sections of the flow.

It is worthy to note that the measured refractive field seems to match better with the simulation data compared with the results from run 178. This could be due to variance in the HXT run condition itself and because Run 179 was much closer to the targeted run condition than Run 178.

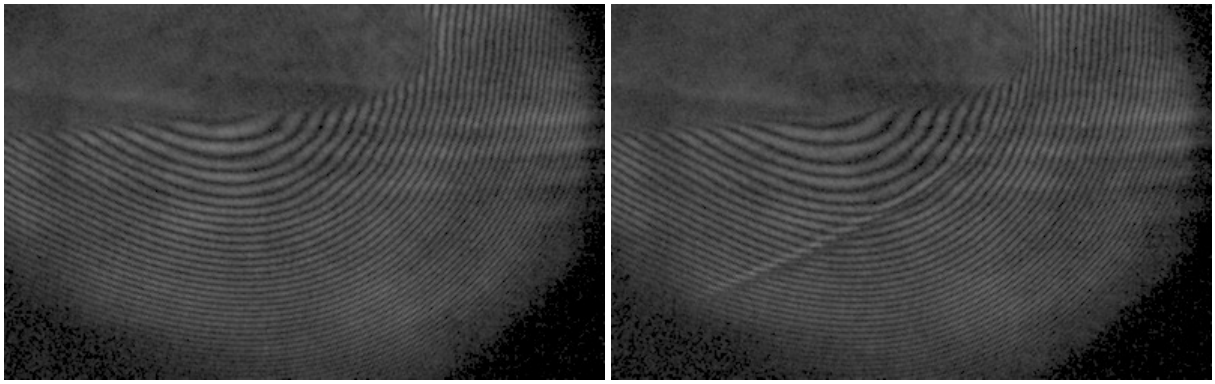

(a) Reference (b) Test

Figure 3.17: Run 179 image captures

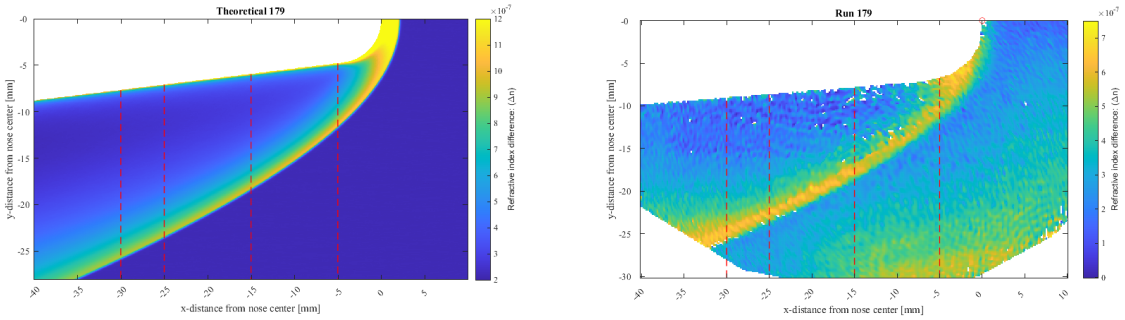

(a) Predicted (b) Measured

Figure 3.18: Run 179 refractive fields: predicted vs measured

In summary, the data collected from these experiments showed good agreement with the theoretical model.

3.3 Test Campaign 3: Hypersonic flow of O2/Ar Mixture, and Pure Argon flow

This test campaign focuses on a 20% Oxygen 80% argon mixture to study how the refractive index field changes as molecular oxygen undergoes nonequilibrium effects and dissociation. A mixture of oxygen and argon was chosen to mimic the oxygen concentration in air and also allow safe operation of HXT. Three run conditions were chosen for this campaign to observe three unique forms of flow. Each run condition was to be observed twice at a far-field FOV measuring

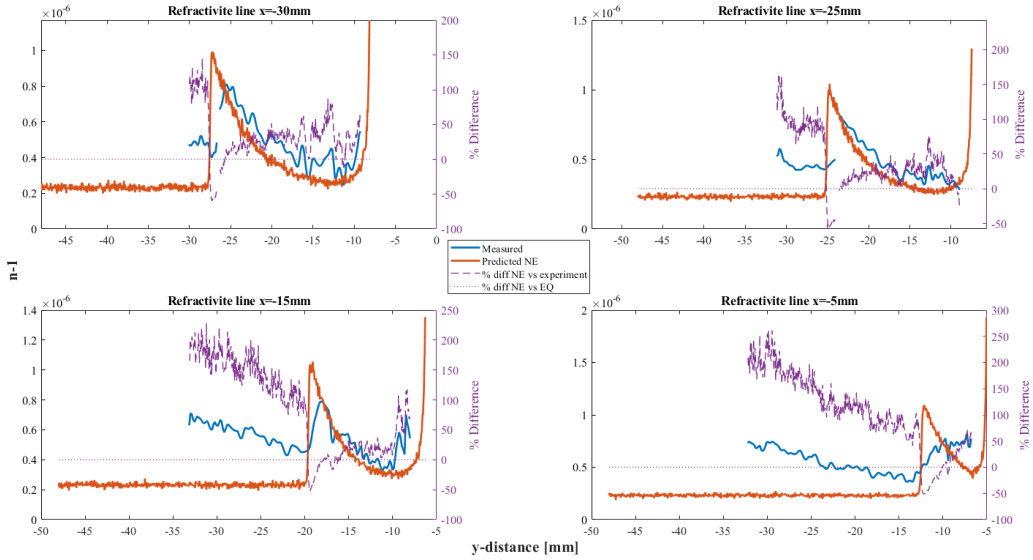

Figure 3.19: Run 179: Refractive index comparison

40mmx64mm, and once at a near-field FOV measuring 16mmx25mm. The far field of view is important for establishing a broad view of the refractive index change in different regions of the flow. A close field of view of the nose is important for allowing a high resolution capture of the data near nose. Figure 3.20 shows the difference between the close and far FOVs.

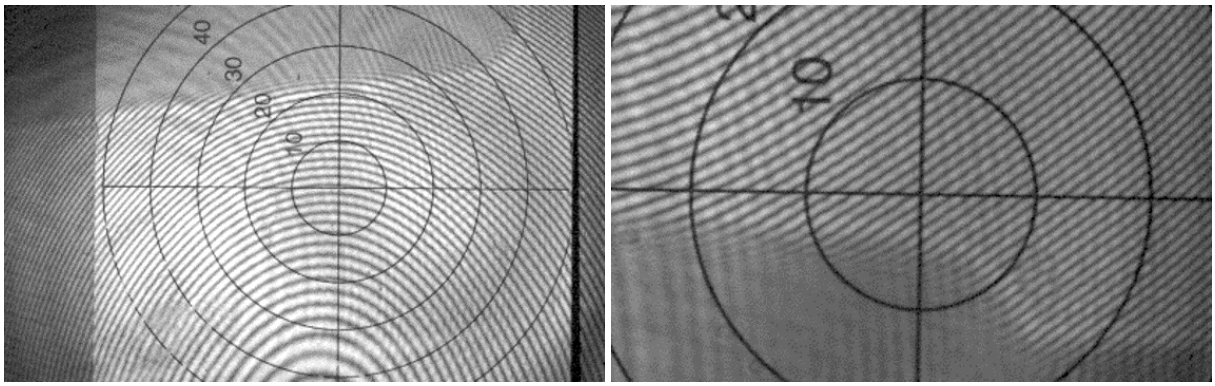

(a) Far FOV: 40x64mm (b) Close FOV: 16x25mm

Figure 3.20: FOVs for Test campaign 3

Table 3.3 shows the run conditions for test campaign 3. The M=7 run was chosen to explore practically equilibrium conditions with no dissociation and only low vibrational nonequilibrium. At M=10 flow will be in the conditions of vibrational nonequilibrium, particularly near the nose and in the boundary layer. At M=15, the molecular oxygen should dissociate especially near the nose of the test article.

	M=7	M=9.8 (highT)	M=10	M=15
M	7.0	10.0	10.0	15.1
Re $[1 \times 10^6]$	2.26	0.76	0.70	0.70
T [K]	228.5	490.8	251.0	236.6
$\rho\,[1 \times 10^{-3}\frac{kg}{m^3}]$	17.1	4.9	3.9	2.5

Table 3.3: O2/Ar runs aimed for in HXT

Data was collected from the successful runs presented in Table 3.4. An argon run was conducted to validate that the polarizability value taken from the literature is a good fit for the experiment. The other O2/Ar runs require the polarizability of argon to be well-known since it consists 80% of the flow.

Type	M=7			M=10			M=15		
Composition	O2/Ar		Ar	O2/Ar		Ar	O2/Ar		Ar
FOV	Far	Close	Far	Far	Close	Far	Far	Close	Far
Run #	204	205	208	200	210	209	202	206	207
M	7.0	7.1	7.0	9.8	9.9	9.8	15.2	15.1	15.0
Re $[1 \times 10^6]$	2.23	2.22	2.35	0.764	0.749	0.757	0.707	0.713	0.737
T [K]	232.1	229.3	235.3	488.1	496.1	513.3	226.2	238.9	236.6
$\rho\,[1 \times 10^{-3}\frac{kg}{m^3}]$	16.85	16.64	17.9	5.00	4.85	4.96	2.46	2.53	2.67

Table 3.4: Successful real run conditions from test campaign 3

3.3.1 Run 209: M=10 Pure Ar capture and post-processing

Figure 3.21 shows the capture from run 209. This capture had a significant amount of jitter to the flow compared with the nitrogen runs. This unsteadiness indicates a potential source of error from the free-stream condition itself.

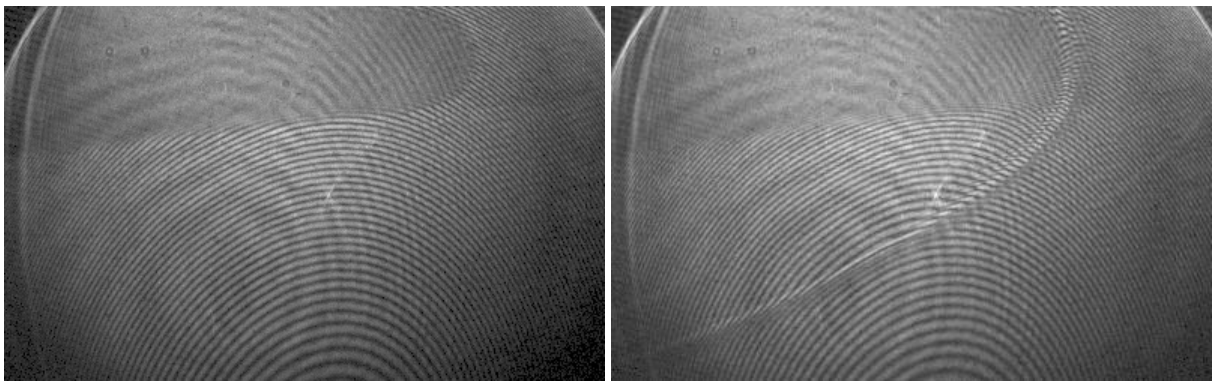

(a) Reference (b) Test

Figure 3.21: Run 209 image captures

For these flows that appear unsteady, it is helpful to qualify how the flow changes with time. The only data that is collected during test time from HXT is the pressure data. This is what determines the run conditions and provides a metric for whether the test condition was captured within the testing window. Figure 3.22 shows the data captured from Run 209 was completely within the testing window (generally indicated by a local minimum in the nozzle static pressure trace), but there were some variations in the pressure during this time. These small pressure variations shows the unsteadiness of the flow during the experiment. While the pressure did not change significantly, this had a significant impact on the tail of the shock wave, which could be seen moving on the order of millimeters during test time.

Postprocessing this run was difficult due to the discontinuity at the shockwave and the fine nature of the fringes. Figure 3.23 shows the difference between the predicted and measured plot from this run. Even though the fringe quality appears quite clear, the camera resolution was insufficient

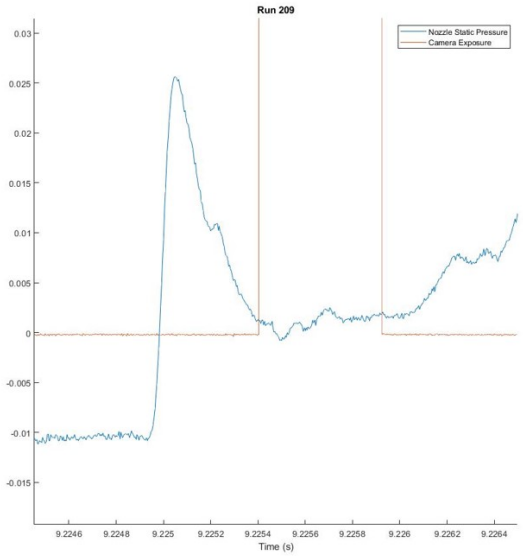

Figure 3.22: Run 209: nozzle pressure trace with capture window overlaid

at such small scales. The phase shift seems to blur through the shock wave.

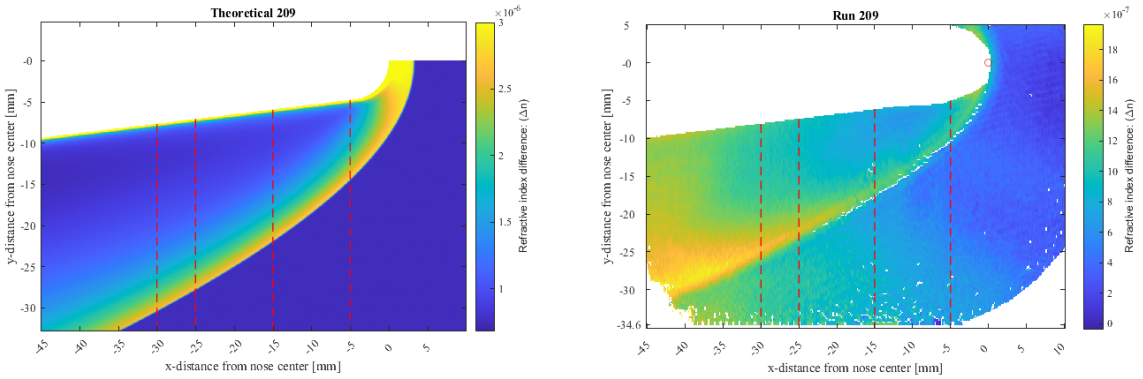

(a) Predicted (b) Measured

Figure 3.23: Run 209 refractive field comparison

It is clear that the shock wave angle is different between the prediction and the actual observation. As a result, the percent difference between the measured and predicted refractive index

fields are very different from each other. The relative maximum values seem to still occur on the same level as predicted, but they occur at a different location due to the different angle of the shock wave. The reason for this will also be discussed in the following section. A comparison between the cross sections is given in Fig. 3.24.

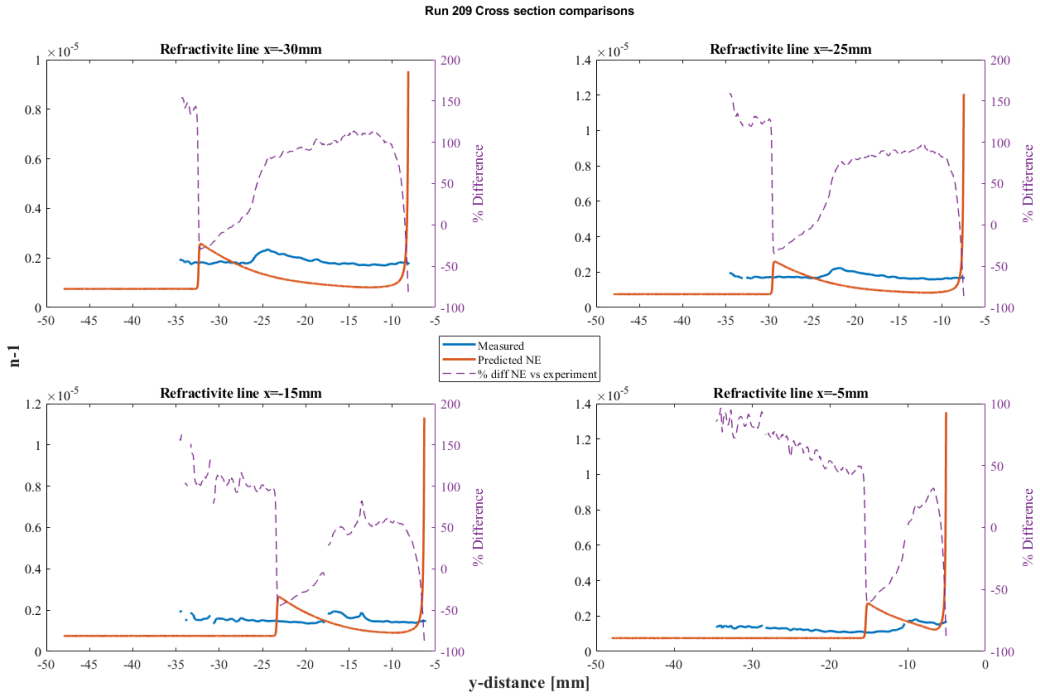

Figure 3.24: Run 209 cross section comparison

4. DISCUSSION

The data presented from earlier will be discussed in detail within this chapter. Uncertainties are considered to describe the difference between the predicted and measured refractive index values. The process to determine the refractive field requires a number of steps, where each step is subject to some uncertainty. Figure 4.1 shows the schematic of all computational and experimental effort involved in the analysis of the refractive index field.

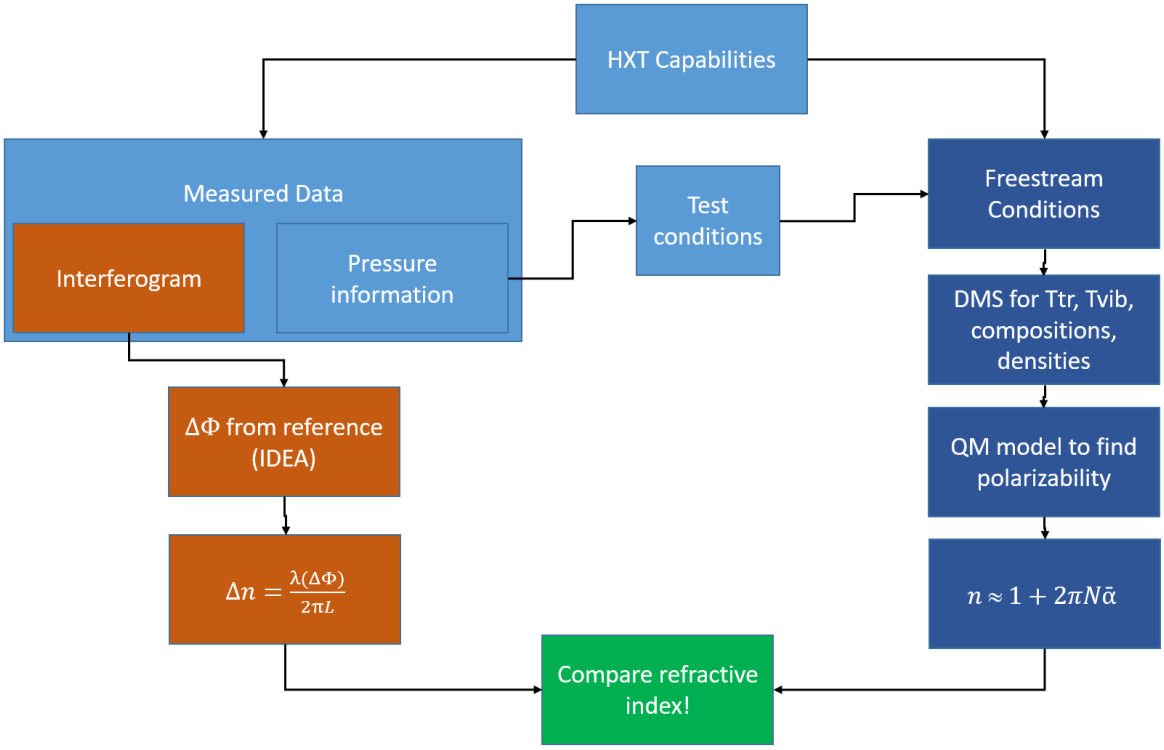

Figure 4.1: System diagram for refractive index field analysis

4.1 Results

4.1.1 Test campaign 1

Run 140 and Run 141 were the first runs of the test campaign, where hypersonic flow over a double wedge test article and Mach stem formation were observed. These runs provided an introduction to testing with HXT and exposed the limits for interferometry: flows that are too optically dense are difficult to extract useful phase data from. Furthermore, low-quality fringe captures are nearly impossible to track in these experiments.

Runs 142 and 143 showed that the refractive index could be measured with high-contrast fringes and also proved that IDEA can be used as a tool to capture small deviations in the phase. There exists some uncertainty in the formation distance of the Mach stem, which makes it difficult to compare the refractive index with respect to the nose tip of the simulated model. In addition, the exact conditions of the Mach stem are more difficult to calculate, since they result from a set of oblique shock waves which form far downstream of the initial disturbance. The exact solution to this formation is computationally expensive, and it could compound the uncertainty of the model, since small deviations in the initial flow conditions affect the flow much more significantly. During experiments where the Mach stem was captured, it would typically shift its position by a few millimeters for the duration of the testing window. This is due to uncertainty from the HXT free stream itself. Despite this, a qualitative validation for small phase change measurements with IDEA has been obtained.

The calculated difference between an equilibrium calculation, which assumes $T_\nu = T_{tr}$, and a nonequilibrium calculation was plotted to show the expected difference at any point in the flow field. Figure 4.2 shows the percentage difference between the flow in thermal nonequilibrium vs equilibrium. Since the temperatures are too low to observe any significant N2 dissociation, there are no effects associated with chemical nonequilibrium.

Notice the total percent difference within the entire flow can only range 2% from an equilibrium and nonequilibrium flows. Run 143 was sampled approximately 95mm away from the nose center,

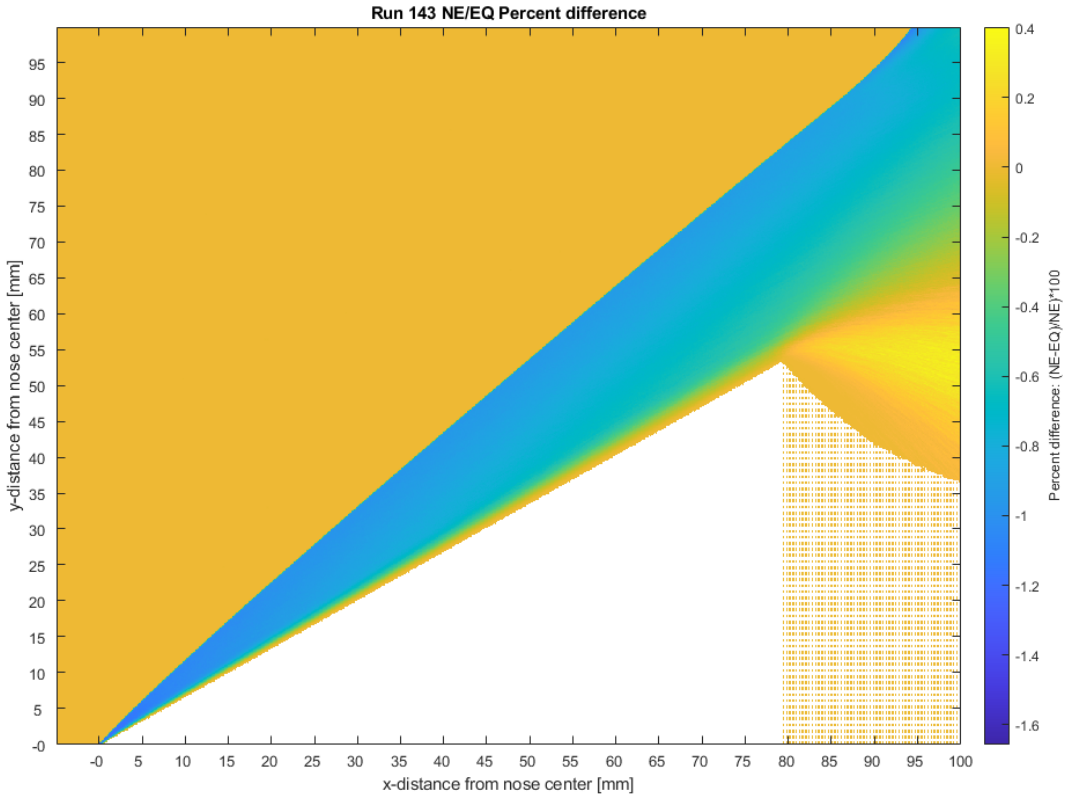

Figure 4.2: System diagram to compare refractive field

so at the top right edge of Fig. 4.2. The difference across the oblique shock wave at that section is approximately 1%, which is not significant enough to measure in the experiment. In addition, the exact location of the experimental observation was not measured precisely, so it is not possible to make a perfect comparison between the measured values and the theoretical ones. However, the plot in Fig. 3.9 shows a similar refractive index field extracted from measurements. The data from test campaign 1 showed that the Michelson interferometer design is sufficient for capturing quantifiable refractive index fields as long as the fringe pattern has good visibility. The next goal was to perform higher enthalpy runs to observe thermochemical nonequilibrium.

4.1.2 Test campaign 2 and 3

For these campaigns, the blunt body test article was used. The post-shock region consistently shows a higher refractive field than predicted, according to experimental data from Run 178 (Fig. 3.16). The difference between the calculated and measured refractive index field increases significantly after the shock front. The source of this difference could either be due to an uncertainty in the HXT run conditions itself or due to a retrace error from the beam. A retrace error would mean the beam is not returning at the exact same path through the tunnel as when it entered (hence it does not retrace the initial line). This would blur the effects of the shock wave through a section of the image. But this is likely not the source of the error, since run 179 did not show that same error, as shown in Fig. 3.19. The path through the HXT was not changed between the tests, so the same retrace error should exist if that were the cause. It is more likely the HXT produced a more ideal run condition for run 179, which is further supported by the fact that the intended run condition was much closer to the run condition measured from the tunnel in 3.2. The effects of vibrational nonequilibrium is very small and can not be measured at the current run conditions, as can be seen in 4.3.

The sampled cross sections show a maximum of 0.5% difference between the refractive index of the flow in vibrational nonequilibrium and equilibrium. The most significant difference occurs near the nose surrounding the first 5mm in front of and behind the wedge nose. Even at at the nose tip region, the difference is 1% maximum, which is not significant enough to be measured. The difference decreases significantly after the normal shock wave.

The hypersonic flow of argon from test campaign 3 does not match the shock wave angle predicted by the high fidelity DSMC simulation. As a result, an accurate comparison of the measured and simulated refractive index field can not be provided. This leads to the need for an detailed uncertainty analysis presented in the following section.

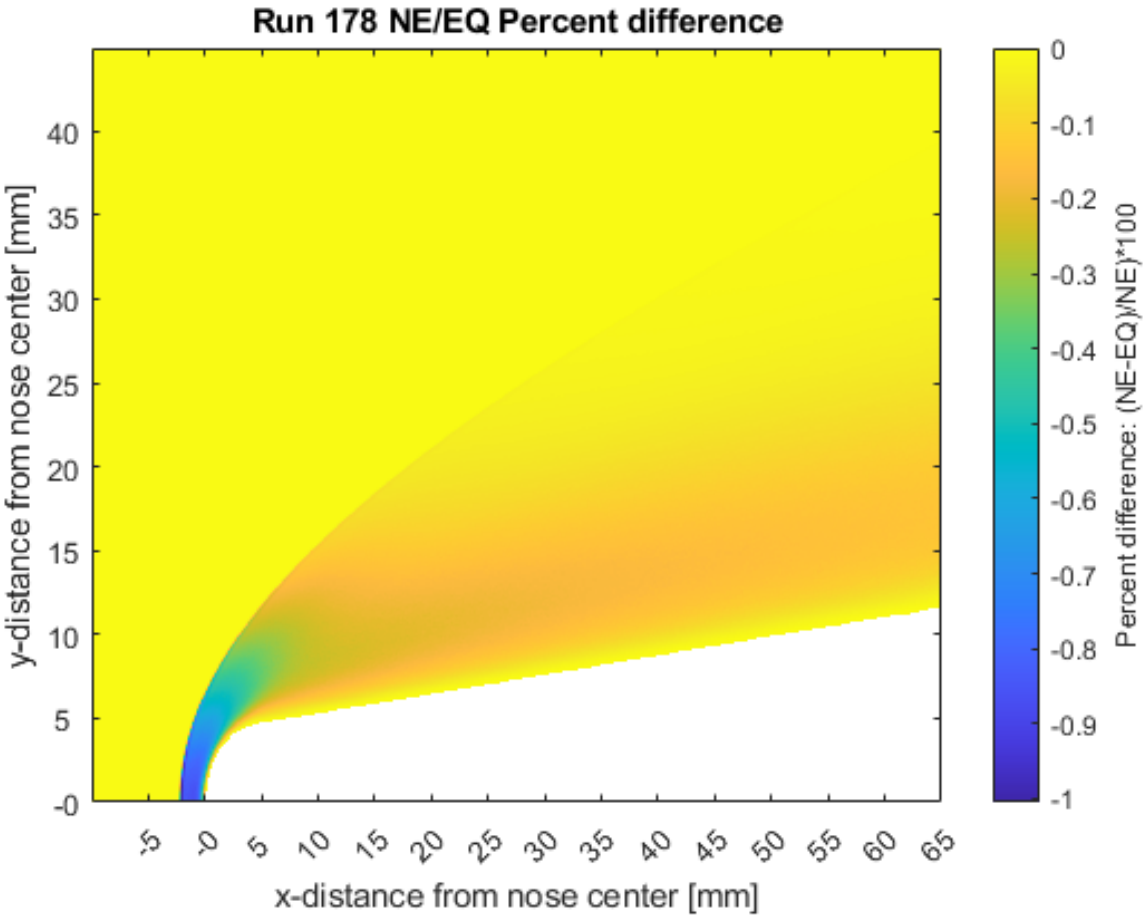

Figure 4.3: Polarizability vs Temperature Run 179

4.2 Uncertainty review

Uncertainty can stem from any of the systems depicted in Fig. 4.1. Each of these uncertainties are discussed in this section to rationalize the difference between experimental results and the theoretical model.

4.2.1 HXT

The HXT is a shock tube that has novel methods for producing supersonic flow for short durations. There are certain aspects of uncertainty that has yet to be quantified, such as viscous effects, which lead to a growing boundary layer along the edges of the tube and decrease the area ratio used to predict the run conditions. The HXT currently does not measure the temperature or pressure in

the test section during test time to verify the exact run conditions, so the flow field variables are calculated using the initial conditions of the tube. However, there are some uncertainties that have been quantified for these experiments. The chemical compositions of the pure N2 runs 178-179 have a 0.36% uncertainty due to the purge/fill process used to prepare the test section. The chemical composition of pure argon Run 209 has an uncertainty of 0.6% for the same reason. The shock speed for any of these runs has up to a 15% uncertainty, which can affect the Mach number and other flow variables as well. The uncertainty due to the shock speed and chemical composition explains the differences in the refractive index field observed in Run 178-179, but it seems unlikely to be the reason for the difference in the predicted and calculated shock wave angle observed in Run 209.

4.2.2 DSMC Simulation

Is is important to note that the DSMC model was established for steady-state flow. This condition is not truly attained in the experiments, since the shock front is shown to jitter throughout test time. There is no good quantification for the unsteadiness of the flow during test time other than the fact that it can be observed by shock wave motion.

The simulations from Run 178 and Run 179 were similar, and they can be compared to each other to gain an understanding of the scale of error from the calculations. Figure 4.4 shows the difference in refractive index between the two run conditions listed in Table 3.2.

Because the simulations use a stochastic method to generate the temperatures at any point in the flow, this introduces some small amounts of noise in the model due to small fluctuations in temperature and other flow parameters. The difference plots in the freestream region from Fig. 4.4 should be uniform if there was no noise in the simulation itself. But when observed at a larger scale, these differences are smoothed out and uncertainty associated with this noise is negligible. The only relevant differences between the two simulated runs, as shown to average 2% by the percent difference plot, is the refractive index field significantly downstream from the tip of the nose. This means the differences in density are only significantly different from the random noise generated by the stochastic model downstream of the nose. This also provides evidence that small

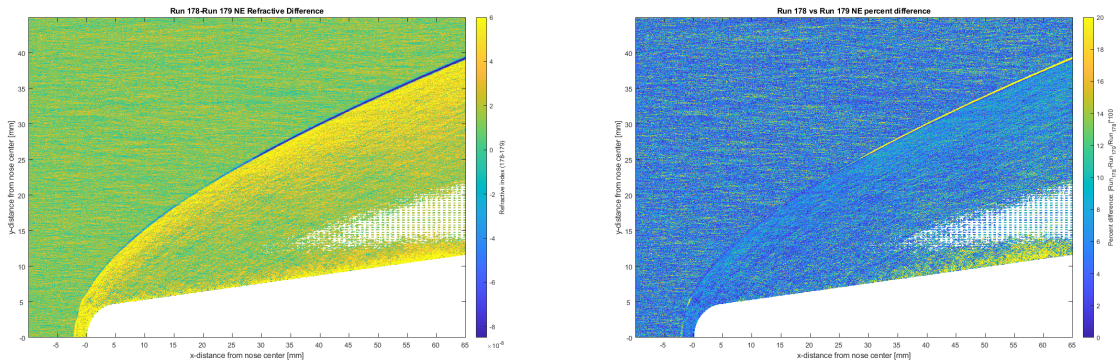

(a) Absolute difference (b) Percent difference (Run 178 values baseline)

Figure 4.4: Difference in refractivity between Run 178 and Run 179

fluctuations in the free-stream in the HXT should likely not affect the refractive index field near the nose significantly for the hypersonic flow of nitrogen.

4.2.3 QM model

The biggest source of uncertainty with the model is the uncertainty in the bias, which is used to account for transitions from the ground state to high-lying electronic states and oscillator strengths and Franck-Condon factors, associated with these transitions, which can not be found in the literature. The model incorporates a constant to account for the unknown oscillator strengths. The presented model also does not take into account rotational nonequilibrium, which was shown to present in the flows, according to the DSMC calculations. But the presence of rotational nonequilibrium has been shown to have much less impact on the polarizability, especially compared to effects associated with the vibrational nonequilibrium.

These differences should only affect the uncertainty in the polarizability calculations for diatomic molecules such as Nitrogen and Oxygen. Simulations of the refractive index field of the hypersonic flow of argon, since the gas is atomic, do not have such uncertainties. Thus the discrepeancy in the shock wave angle and associated refractive index differences can not be explained by any uncertainties in the QM model.

The polarizability model for the molecular nitrogen, which is used to calculate the refractive

index, was validated in an earlier work by Tropina [1]. The dependence of the polarizability on the translational temperature for the run 178 conditions is shown in Fig. 4.5.

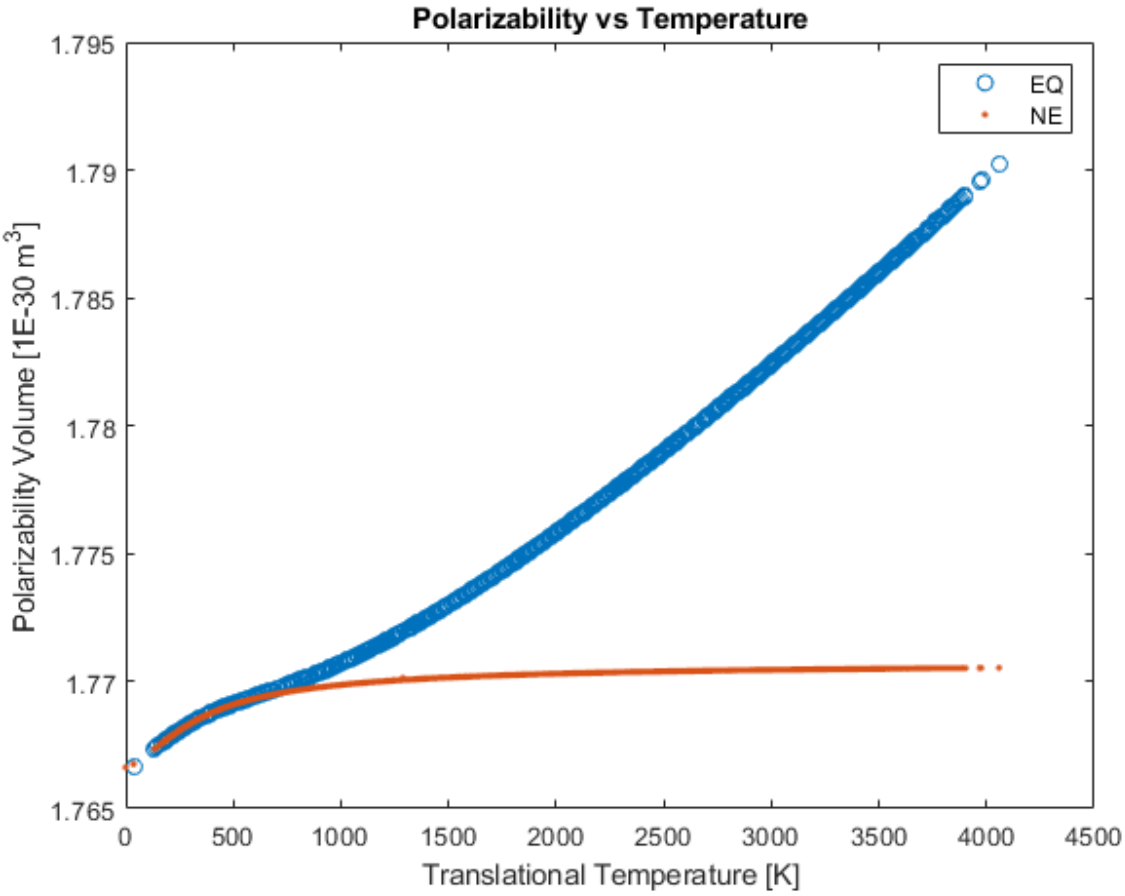

Figure 4.5: Polarizability vs temperature from simulated Run 178

There is further validation of the QM approach of calculating the polarizability, performed in a recent work. Simulations of nitrogen and oxygen at M=8.5 were performed in [25]. An important finding from that work indicates the vibrational and rotational degrees of freedom of molecules may lead to appreciable increase in the observed polarizability in molecular nitrogen and oxygen, particularly more for molecular oxygen.

4.2.4 Experimental sampling

Experimental sampling requires the use of some assumptions to perform reasonable calculations. The test article was assumed to be aligned perfectly perpendicular to the flowfield generated by HXT. This is a fairly reasonable assumption since the slots on the test article only allow for .02" of wiggle room around each of the eight bolts that holds the wedge in place. Another assumption is that the beam is sampling the test article perfectly normal to the cross section. During test campaign 2, this was only verified by a general inspection of the HXT window during alignment, so Run 178-179 may be susceptible to this error. Test campaign 3 used a more accurate alignment tool to decrease the uncertainty to within 3mm away from the center over the 68" span of HXT (which relates to 0.1 degrees of view angle uncertainty). In addition to the quantification of these uncertainties, it is also apparent that the shockwave is being viewed at a normal angle, since any non-normal angle would visibly thicken the shockwave.

Due to the use of a Michelson interferometer, another source of uncertainty develops in the case of retracing the same path in the return beam as the entering beam through the test section. Run 178-179 tests did not incorporate a valid way to quantify how well retracing was performed, but Run 209 did with the advent of the grate alignment method, discussed in section 3. This was a significant improvement and accurately verified the uncertainty in the return angle and collimation of the beam. The path retracing for Run 178-179 must be reasonably close, since otherwise a double-image would be viewed of the shoc kwave–one visible from the beam entrance path and one from the return path.

Another assumption about the measurements is that the flow is uniform across the span of the test article. In reality, some turbulence will be generated at the edges of the wedge, but this should be negligible over the 16" span of the test article. Outside of the 16" span, the flow is assumed to be uniform from the 37" nozzle diameter exit from HXT. This has some unquantifiable uncertainty, as it is assumed the flow exiting the nozzle comes as a nonexpanding column of air. In reality, some small amounts of expansion may occur, but these are assumed to be negligible. These effects are almost certainly negligible compared to the area affected by the test article.

Some measurements important to the OPD equation (1.13) are also sources of uncertainty. The wavelength of the light is assumed 532nm, but there is a small uncertainty in the linewidth, which measures the range of frequencies the laser outputs. The uncertainty in the linewidth is small because the continuous-wave laser is used to create the nanosecond-scale pulses. The test article was manufactured to a 16" span with a tolerance of ±0.05", which shows the small uncertainty in the optical path for the laser.

The biggest source of uncertainty comes from measuring the phase of the flow. The nature of a shock wave introduces a sharp discontinuity that makes it difficult to track fringes as they move across. Algorithms, such as IDEA, have a difficult time discerning these fringes, especially when the fringes are near the same thickness as the resolution of the camera. The Shimadzu HPV-X2 camera has a 400x250 pixel resolution, which relates to 6 pixels/mm for the far FOV and 15pixels/mm for the close FOV. Sub-millimeter differences are difficult to resolve at the far FOV because of this, especially in regions where the phase appears to blur due to the shock front. Phase shifts on the order of multiple fringes (multiple 2π shifts) are therefore difficult to fully discern, especially since the blurring at the discontinuity can naturally trick the human eye into following a false fringe, blurred by the resolution limits of the camera. Run 209 is predicted to change by more than 2π, which could explain some of the difficulty in measuring the refractive change across the shock wave.

Vibrations and small fluctuations in the laboratory environment also introduce uncertainty into the measurements. An analysis was made during test campaign 1 to quantify the steady-state error due to these fluctuations. This was an average designed to encapsulate errors caused by fluctuations in the lab environment and other small disturbances that could occur during test time. The results from the study showed the amount of expected error from the measurements within one standard deviation is approximately 0.3 radians. This relates to a 3e-8 uncertainty in the refractive field due simply to variations caused by the static laboratory environment (this also factors in the uncertainty in wavelength, since that affects the fringes as well). Figure 4.6 shows the steady-state error taken over numerous captures to quantify the amount of phase error expected from any given

measurement.

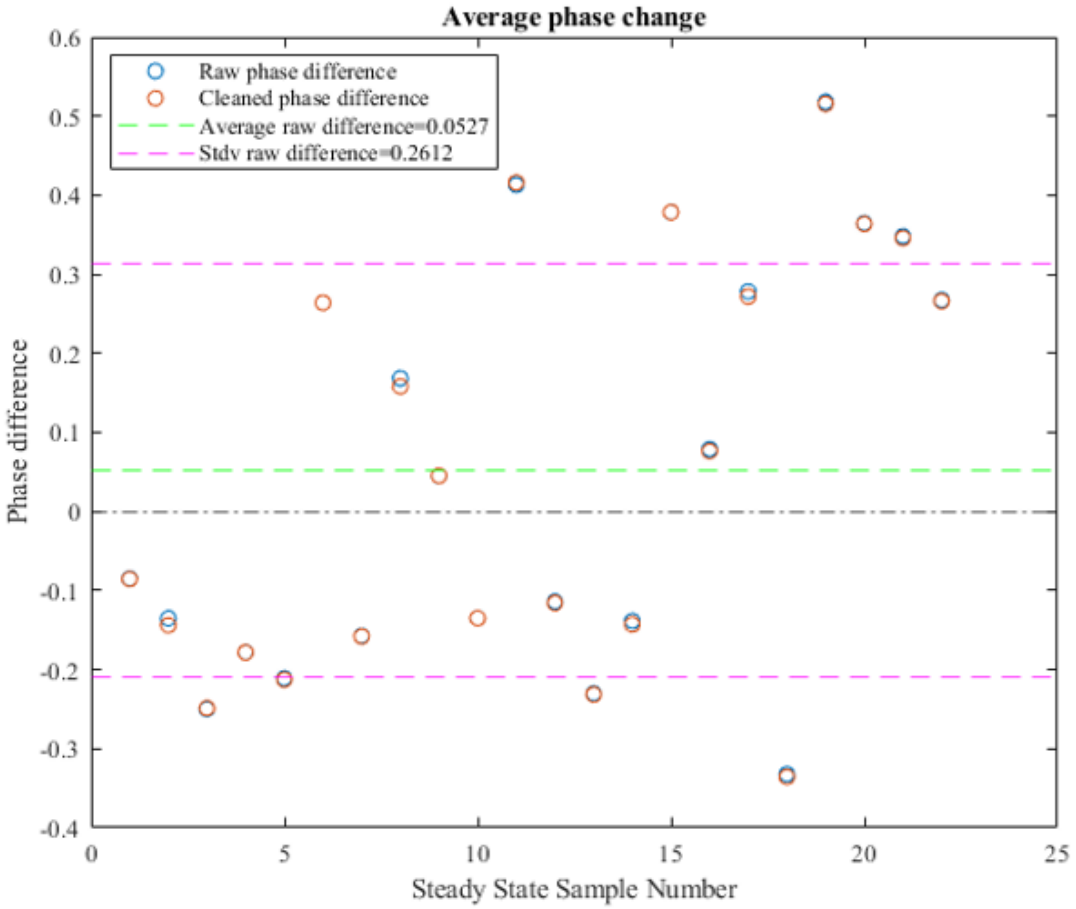

Figure 4.6: Steady State error from test campaign 1

For tests which expect to measure refractive changes on the order of 10e-7, this relates to a 3% uncertainty. Notice Run 178-179 should expect this uncertainty (see Fig. 3.15), while Run 209 should only expect half of this uncertainty (Fig. 3.24). The higher the jump in the refractive index, the less uncertainty there is due to laboratory fluctuations, but the more difficult it becomes to track the phase shift across the shockwave. The size of the test article can be controlled for different experiments by limiting the refractive index jump to 2π as shown in the OPD equation 1.13. The test article size can be adjusted to ensure the phase shift does not exceed 2π based on

the simulated refractive field change.

An example is shown here to see how measuring the discontinuity is an essential but difficult task of the measuring process. An initial analysis of Run 179 produced a phase change diagram that appears significantly different from what is currently accepted as the refractive field for the run. Figure 4.7 shows how the filtering process with IDEA can lead to a large impact on the refractive index, due to phase uncertainty. The difficulty to measure the refractive index leads to an uncertainty that can be large and difficult to quantify, particularly if the phase shift is multiple 2π, which shifts the fringe pattern at a smaller scale than the camera resolution can resolve.

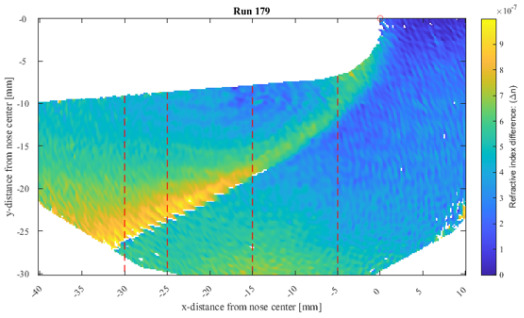

(a) Initial refractivity plot

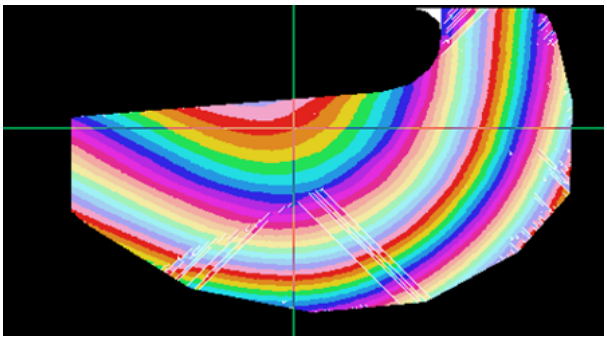

(b) Initial IDEA 2D scan

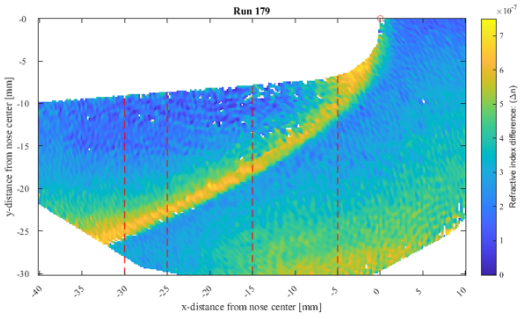

(c) Final refractivity plot

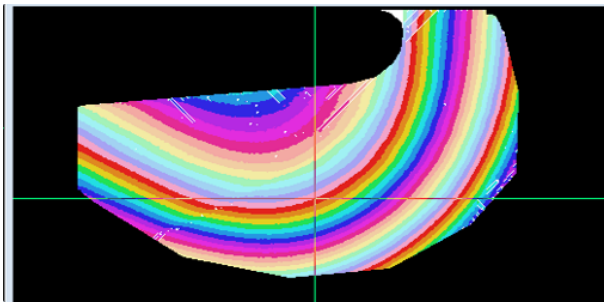

(d) Final IDEA 2D scan

Figure 4.7: Run 179: phase measuring uncertainty

Finally, there are uncertainties which can not be qualitatively evaluated at this step. One of the inherent issues with the current method used to measure the phase shift is the fact that it is

based on a peak-to-valley measure of the intensity. The single interferogram is represented by pixels with varying intensity levels. The peak with the greatest intensity is considered to be the most in-phase, whereas any peaks less than that intensity will be considered to deviate by some phase to cause that decrease in intensity. The issue with this is it necessitates a flat-top distribution of the laser beam intensity , which was never fully achieved in any of the data captures. This means the light intensity is not uniform everywhere on the beam. Differences in the laser intensity become confounded with differences in phase due to the peak-to-valley method employed by the algorithm. Unfortunately, there is no way to switch to another algorithm without changing how the data is collected/sampled. To work around this issue, the bright/dark portions of the fringe pattern can span multiple pixels, so the peaks are smoothed out appropriately. Also, much of the phase difference uncertainty is removed by subtraction from the reference image. The reference image bakes-in the error due to the intensity profile of the original fringe pattern. There also exists some uncertainty due to internal reflections from the non AR-coated windows in HXT. This introduces some fine fringe lines which are generated by the reflections off the windows, but they should be mostly filtered out from the FFT algorithm.

4.3 Future developments

It is nessesary to have a measured quantification of the test-time flow variables to limit the uncertainty in HXT testing parameters. For better understanding of vibrational nonequilibrium, future test campaigns must include vibrational temperature and vibrational states population measurements, since they can quantify the level of vibrational nonequilibrium experienced in the flow.

The biggest priority in improving the interferometer will be fixing the issue of the curved fringes, since that will reduce the difficulty in measuring the phase change through the discontinuity with IDEA. This was partially achieved during test campaign 3 with the close field of view runs, which were a small enough field of view to employ a mirror tilt which showed nearly parallel fringes. It may also be desirable to restrict testing to the close field of view, since the largest amounts of vibrational nonequilibrium occur close to the nose, and the large field of view serves mostly to confirm locations in equilibrium.

For further development of the interferometer-based refractive index measurements in high speed flows, it would be worthwhile to look at developing a phase-shifting method to capture interferograms for analysis. This has been the more common method of measuring accurate interferograms since the 1970s, when computing and digital cameras were much more accessible. Phase-shifting analysis uses image contrast to obtain phase information, which is different than the current method, which uses peak-to-valley image intensity to find the phase. An added benefit is that the phase-shifted interferograms would be collected simultaneously, so there would be no need to reference an initial image. A drawback of collecting data with phase-shifting interferograms is part of the same reason it is appealing: multiple interferograms would need to be collected simultaneously. The high-speed camera is only capable of a 400x250 pixel resolution, and four interferograms would need to be taken in that space. This reduced resolution may be counteracted by the improved accuracy per fringe line due to the phase-shifting algorithm and the elimination of intensity errors from the peak-to-valley method.

4.4 Conclusion

The refractive index field of hypersonic flows over a double-wedge and blunt-body wedge test article was studied at different gas compositions. The Michelson interferometer set up was developed to measure the phase change and refractive index difference over a range of test conditions and Mach numbers. A theoretical model was validated and used to compare the measured and calculated refractive index field. Good agreement between the experimental and computational data for the hypersonic flow of nitrogen at M=8.5 was shown. The calculated difference in the refractive index due to vibrational nonequilibrium was around 2%. Detailed analysis of experimental and numerical uncertainties was performed.

REFERENCES

[1] A. A. Tropina, Y. Wu, C. M. Limbach, and R. B. Miles, "Influence of vibrational non-equilibrium on the polarizability and refraction index in air: computational study," *Journal of Physics D: Applied Physics*, vol. 53, p. 105201, dec 2019.

[2] J. D. Anderson, *Hypersonic and high-temperature gas dynamics*. American Institute of Aeronautics and Astronautics, Inc, 2019.

[3] R. C. Millikan and D. R. White, "Systematics of vibrational relaxation," *The Journal of Chemical Physics*, vol. 39, no. 12, pp. 3209–3213, 1963.

[4] J. G. HALL, A. Q. ESCHENROEDER, and P. V. MARRONE, "Blunt-nose inviscid airflows with coupled nonequilibrium processes," *Journal of the Aerospace Sciences*, vol. 29, no. 9, p. 1038–1051, 1962.

[5] L. E. Mackey and I. D. Boyd, "Assessment of hypersonic flow physics on aero-optics," *AIAA Journal*, vol. 57, p. 3885–3897, Sep 2019.

[6] P. W. Atkins and R. Friedman, *Molecular quantum mechanics*. Oxford University Press, 2011.

[7] E. Zipf and R. McLaughlin, "On the dissociation of nitrogen by electron impact and by e.u.v. photo-absorption," *Planetary and Space Science*, vol. 26, no. 5, pp. 449–462, 1978.

[8] W. Chan, G. Cooper, R. Sodhi, and C. Brion, "Absolute optical oscillator strengths for discrete and continuum photoabsorption of molecular nitrogen (11–200 ev)," *Chemical Physics*, vol. 170, no. 1, pp. 81–97, 1993.

[9] R. H. Huebner, R. J. Celotta, S. R. Mielczarek, and C. E. Kuyatt, "Apparent oscillator strengths for molecular oxygen derived from electron energy-loss measurements," *The Journal of Chemical Physics*, vol. 63, no. 1, pp. 241–248, 1975.

[10] W. Chan, G. Cooper, and C. Brion, "Absolute optical oscillator strengths for the photoabsorption of molecular oxygen (5–30 ev) at high resolution," *Chemical Physics*, vol. 170, no. 1, pp. 99–109, 1993.

[11] P. H. Krupenie, "The spectrum of molecular oxygen," *Journal of Physical and Chemical Reference Data*, vol. 1, no. 2, pp. 423–534, 1972.

[12] B. J. Hoenders, "The painful derivation of the refractive index from microscopical considerations," *Lecture Notes in Electrical Engineering*, p. 297–305, 2008.

[13] H. Kragh, "The lorenz-lorentz formula: Origin and early history," *Substantia*, p. 1–18, Jul 2018.

[14] R. R. Boyce, J. W. Morton, A. F. P. Houwing, C. Mundt, and D. J. Bone, "Computational fluid dynamics validation using multiple interferometric views of a hypersonic flowfield," *Journal of Spacecraft and Rockets*, vol. 33, no. 3, pp. 319–325, 1996.

[15] P. Psota, G. Çubreli, J. Hála, D. Šimurda, P. Šidlof, J. Kredba, M. Stašík, V. Lédl, M. Jiránek, M. Luxa, and J. Lepicovsky, "Characterization of supersonic compressible fluid flow using High-Speed interferometry," *Sensors (Basel)*, vol. 21, Dec. 2021.

[16] J. M. Desse and E. Fabre, "Differential interferometry for studying hypersonic flows," *Experiments in Fluids*, vol. 20, no. 4, p. 273–278, 1996.

[17] E. P. Goodwin and J. C. Wyant, *Field Guide to Interferometric Optical Testing*. SPIE Press, 2006.

[18] X. Qing, J. Guowang, Z. Caiying, W. Zhengde, H. Yu, and Y. Peizhang, "The filtering and phase unwrapping of interferogram," 2004.

[19] K. Creath and J. Schmit, "Interferometry | phase-measurement interferometry," *Encyclopedia of Modern Optics*, p. 364–374, 2005.

[20] K. H. Womack, "Interferometric Phase Measurement Using Spatial Synchronous Detection," *Optical Engineering*, vol. 23, no. 4, p. 234391, 1984.

[21] S. J. Plimpton, S. G. Moore, A. Borner, A. K. Stagg, T. P. Koehler, J. R. Torczynski, and M. A. Gallis, "Direct simulation monte carlo on petaflop supercomputers and beyond," *Physics of Fluids*, vol. 31, no. 8, p. 086101, 2019.

[22] M. Hipp, J. Woisetschläger, P. Reiterer, and T. Neger, "Digital evaluation of interferograms," *Measurement*, vol. 36, no. 1, pp. 53–66, 2004.

[23] G. Hollows and N. James, "Understanding focal length and field of view: Edmund optics."

[24] "Basic lens selection: Edmund optics."

[25] B. I. Lukhovitskii, A. S. Sharipov, I. V. Arsent'ev, V. V. Kuzmitskii, and O. G. Penyazkov, "On the refractive index of a gas under high-thermal-nonequilibrium conditions," *Journal of Engineering Physics and Thermophysics*, vol. 93, no. 4, p. 850–857, 2020.